

RICE UNIVERSITY

**Efficient Two-fluid Hydrodynamic Simulations of
Impulsively Heated Coronal Loops**

by

Will T. Barnes

A THESIS SUBMITTED
IN PARTIAL FULFILLMENT OF THE
REQUIREMENTS FOR THE DEGREE

Master of Science

APPROVED, THESIS COMMITTEE:

Stephen J. Bradshaw, Chair
Assistant Professor of Physics and
Astronomy

David Alexander
Professor of Physics and Astronomy

Marjorie Corcoran
Professor of Physics and Astronomy

Houston, Texas

December, 2015

ABSTRACT

Efficient Two-fluid Hydrodynamic Simulations of Impulsively Heated Coronal Loops

by

Will T. Barnes

The coronal heating problem has puzzled physicists and astronomers for nearly a century. While the origin of these surprisingly high temperatures in the upper solar atmosphere is most certainly magnetic,

Contents

Abstract	ii
List of Illustrations	vi
List of Tables	xi
1 Introduction	1
1.1 Structure of the Solar Atmosphere	3
1.2 The Solar Magnetic Field	6
1.2.1 The Solar Dynamo and Flux Emergence	6
1.2.2 Magnetic Reconnection	9
1.3 The Coronal Heating Problem	12
1.3.1 AC Heating	14
1.3.2 DC Heating	15
1.4 Summary	18
2 Coronal Loops	20
2.1 Observations	22
2.2 Modeling	24
2.2.1 Static versus Dynamic	24
2.2.2 Magnetohydrodynamics	24
2.2.3 Hydrodynamics	24
2.3 Summary	24
3 Emission Diagnostics	25
3.1 Spectral Line Intensity	25

3.2	Differential Emission Measure	29
3.2.1	Reconstruction Techniques	30
3.2.2	Scaling Laws	33
3.2.3	Observational Difficulties	37
3.3	Forward Modeling	39
4	Numerical Modeling	43
4.1	One-dimensional Two-fluid Hydrodynamics	43
4.2	“0”-Dimensional Hydrodynamic Models	48
4.2.1	The EBTEL Model	50
4.2.2	The Two-fluid EBTEL Model	54
4.3	Numerical Implementation	60
4.3.1	Euler Method	62
4.3.2	Fourth-order Runge-Kutta Method	62
4.3.3	Adaptive Timestep Routine	64
5	Results	66
5.1	Heating Functions	67
5.2	Electron Heating	72
5.3	Ion Heating	72
5.4	Single-fluid Comparisons	72
6	Conclusions	73
A	Coronal and Transition Region Pressure Gradient Integrals	74
B	Additional Plots	75

Illustrations

1.1 Total eclipse as seen from Svalbard, Norway on March 20, 2015. Open and closed loops in the highly-structured solar corona are clearly visible. Photo courtesy of Miloslav Druckmüller.

1.2 (a) Schematic showing the layers of the solar atmosphere; the corona is the uppermost layer of the atmosphere. Courtesy of NASA (b) Temperature and density as a function of height above the solar surface; the corona is characterized by low densities and anomalously-high temperatures. Taken from Gary et al. (2007) . . .

1.3 (a) Flux emergence from twisted and tangled field below the photosphere yields loop structures that stretch high into the solar atmosphere. Taken from Gold (1964). (b) The coronal magnetic field topology is extremely complex, making determinations of coronal plasma dynamics difficult. Shown here is a magnetic field extrapolation constructed from an optical magnetogram. An image from the TRACE satellite is superimposed to show the loop structures. Taken from Reale (2010).

1.4 Evolution of β as a function of height in the solar atmosphere. In the chromosphere, the gas pressure dominates ($\beta > 1$) while in the corona, the opposite is true and $\beta < 1$, making cross-field motion negligible. Out in the solar wind, the plasma returns to $\beta > 1$. Taken from Gary (2001).

1.5	Cartoon showing basics of reconnection process. Image taken from Priest & Forbes (2000)	9
1.6	(a) Cartoon showing braided flux tubes rooted, or line-tied, to the solar surface. Braiding allows for the build-up and relaxation of the field, providing an energy release mechanism capable of heating the solar corona. Taken from Parker (1983b). (b) Image from the <i>Hi-C</i> sounding rocket mission showing spatially-resolved braided flux tubes in the solar corona. Image taken from Cirtain et al. (2013)	16
2.1	Image captured by the 171 Å channel of the Atmospheric Imaging Assembly (AIA) onboard the Solar Dynamics Observatory (SDO). An arcade of loops in an active region can be seen on-disk in the lower left corner. Several prominent loop structures also appear off-limb on the right side. Image courtesy of NASA/SDO.	21

3.1 (a) Simulated DEM curve and the resulting EM loci reconstruction. From the DEM curve, the plasma is approximately isothermal, being sharply peaked about 1 MK. Correspondingly, the EM loci curves intersect in a region centered on 1 MK, allowing for a well-constrained determination of T_C . Image taken from Landi & Klimchuk (2010). (b) Emission measure distribution reconstruction for an active region core. The colored curves show the emission measure calculation using the EM loci method. The black and red histograms show the DEM(T) dT reconstructed using the MCMC method of Kashyap & Drake (1998). Here, the DEM is multiplied by the temperature bin for comparison with the EM loci calculation. The yellow lines to the left and right of the peak show the cool and hot slope fits in the ranges $6.0 < \log T < 6.6$ and $6.6 < \log T < 7.0$, respectively. Image taken from Warren et al. (2012)	32
3.2 (a) Diagram showing how the loop parameters are mapped to the detector geometry. More emission is concentrated at the ends of the detector array because of the curvature of the loop. (b) Plot of forward-modeled intensity as a function of loop coordinate as observed by the 131 Å channel of SDO/AIA. The upper and lower solid curves represent the total and hot-only emission assuming equilibrium ionization. The dashed curves correspond to non-equilibrium ionization. Both images taken from Bradshaw & Klimchuk (2011).	41

4.1 Schematic showing how a loop half-length, with coronal portion of length L and TR length ℓ , is represented in EBTEL. Note that the loop is shown as a cylinder since (nearly) all effects due to gravitational stratification are ignored. Quantities denoted with a “0” subscript are evaluated at the corona-TR interface; quantities denoted with an “a” subscript are evaluated at the loop apex. Note that the relative size of the TR is exaggerated for the purposes of illustration and in reality $\ell \ll L$	51
4.2 Comparison between EBTEL (dashed) and the 1D hydrodynamic code HYDRAD (solid) for a heating function with randomly chosen start times and amplitudes chosen from a power-law distribution. The upper panel shows the heating profile, the middle panel shows the temperature profiles, and the bottom panel shows the density profiles. For both the temperature and density, the EBTEL profile follows the HYDRAD profile quite closely. For the EBTEL profiles, the apex quantities are shown here. For the HYDRAD profiles, the quantities are averaged over the upper portion of the loop.	52
4.3 Comparisons between the EBTEL-2fl model (dashed) and HYDRAD (solid) for (a) a single triangular pulse lasting 500 s and (b) the same heating profile as in Fig. 4.2. The upper panels show the heating profiles, the middle panels show the electron (blue) and ion (red) temperature profiles, and the bottom panels show the density profiles.	58
5.1 Distribution of event energies for $L = 40$ Mm, $\alpha = -1.5$, $T_N = 5000$ s. While each run only includes ~ 16 events, 625 runs are computed such that $N_{tot} \sim 10^4$. The dashed red line shows the power-law fit to the resulting event distribution. The resulting α value from the fit is in good agreement with the specified value.	70

5.2 All heating functions are for $L = 40$ Mm. Starting counter-clockwise from the bottom left: uniform heating amplitudes for $T_N = 1000$ s; uniform heating amplitudes for $T_N = 5000$ s; power-law distributed heating amplitudes for $\alpha = -1.5$, $T_N = 2000$ s; power-law distributed amplitudes for $\alpha = -1.5$ where the wait times depend on the event energies and the mean wait time for both b values is $\langle T_N \rangle = 2000$ s. . . 71

Tables

2.1 Typical parameters for several different types of loops. Adapted from Reale (2010).	22
3.1 Summary of emission measure scalings from observational and modeling studies. Scalings are typically calculated coolward of the emission measure peak and typically range from 2 to 5. Adapted from Bradshaw et al. (2012)	36

Chapter 1

Introduction

The Sun is the most important celestial body to life on Earth. For the last five billion years, it has provided the light by which humans observe the world around them and the heat to save the planet from the frigid temperatures of interplanetary space. Because of its proximity, the Sun provides astronomers an exclusive and unique look into how stars behave. By observing and understanding the Sun, one can make conclusions about other types of stars in our galaxy and the universe.

Perhaps no other consistent celestial event has attracted as much attention as the solar eclipse. Solar eclipses have been observed and recorded for thousands of years, with some reports dating back to the fourteenth century BC (Golub & Pasachoff, 2010). The recordings of ancient eclipses have been heavily studied. Chinese rock drawings dating back to the Han dynasty (approximately 1900 years ago) appear to show the moon completely obscuring the Sun. Additionally, some have even suggested the Aubrey holes that surround the Stonehenge site were used to track and predict both solar and lunar eclipses (Golub & Pasachoff, 2010). Though some claims of ancient eclipse studies are controversial, it suffices to say that humans have long sought to study and explain the behavior of the nearest star to Earth.

In particular, solar eclipses have captured the attention of artists for centuries.



Figure 1.1 : Total eclipse as seen from Svalbard, Norway on March 20, 2015. Open and closed loops in the highly-structured solar corona are clearly visible. Photo courtesy of Miloslav Druckmüller.

Cosmas Damian Asam, a Bavarian painter and architect active in the early eighteenth century, used images of solar eclipses in many of his works, including several frescoes and an altarpiece. Olson & Pasachoff (2007) discuss how Asam, a deeply religious artist, was commissioned several times to depict the vision of St. Gregory the Great, a Benedictine monk, as described in his work *Dialogues*.

One of these depictions, an altarpiece at a Benedictine monastery in Kladruby, Czech Republic (see Fig. 7 of Olson & Pasachoff (2007)), shows “the visionary globe surrounded by a glowing halo of yellow light that more closely resembles the solar corona” (Olson & Pasachoff, 2007). An additional altarpiece at another monastery in Weltenburg, Germany shows a perhaps even more pronounced depiction of the solar corona during a total solar eclipse. Olson & Pasachoff (2007) note that, given his detailed depictions, Asam must have observed several solar eclipses as well as the

solar corona, with these astronomical events profoundly impacting his depictions of supernatural events in his works. This is but one example of how solar eclipses and their consequential insight into the highly structured solar atmosphere, have shaped scientific and artistic discourse throughout history. maybe here need some info on observing instruments, SDO/AIA, Hinode, Yohkoh, TRACE, IRIS, Hi-C; talk of early observations probably easily transitions into discussion of more modern observations, understanding of the Sun/corona need some sort of wrap-up for this section; maybe also add something here about practical applications/space weather?

1.1 Structure of the Solar Atmosphere

Though the Sun can be easily seen from Earth, its dynamic and highly structured atmosphere is not observable with the naked eye, with the one exception being brief glimpses of the corona during an eclipse. The interior of the Sun is of course very complex and constitutes a very different regime of physics than that seen in the solar atmosphere. Thus, this work will be primarily limited to the upper solar atmosphere with some discussion of the lower layers.

The solar atmosphere is often divided up into four separate regions: the photosphere, the chromosphere, the transition region, and the corona. Fig. 1.2(a) shows a cartoon of the different layers while Fig. 1.2(b) shows the density and temperature profiles of the atmosphere with each region labeled. The *photosphere* is what we typically refer to as the solar surface, with the actual surface located where the

optical depth, τ , is equal to 1. This region also contains the lowest temperature on the Sun, approximately 4400 K, located about 525 km above the surface (Carroll & Ostlie, 2007). The photosphere is where the majority of the visibly (with the naked eye) observable photons originate.

The temperature minimum defines the top of the photosphere above which lies the *chromosphere*. As can be seen from Fig. 1.2(b), the density in the chromosphere is many orders of magnitude less than that of the photosphere and the temperature has increased from the minimum up to about 1×10^4 K. Though not visible with the naked eye, the chromosphere is highly structured. Structures such as spicules, tall columns of gas that extend high into the solar atmosphere thought to heavily impact the behavior of plasma in the corona (De Pontieu et al., 2011), originate in the photosphere as well as filaments, essentially spicules observed on-disk and plage, bright regions surrounding sunspots.

Next is the *transition region*, so called because of the steep temperature and density gradients (see Fig. 1.2(b)) that mark the transition between the chromosphere and the corona. The transition region is extremely thin, only a few hundred kilometers as compared to the chromosphere which extends over many thousands of kilometers. However, in this very short change in altitude, the temperature in the solar atmosphere jumps from $\approx 1 \times 10^4$ K to temperatures exceeding 1×10^5 K.

Finally, the solar *corona*, or “crown”, is the highly-dynamic uppermost layer of the Sun’s atmosphere. Visible with the naked eye only during a total solar eclipse (see Fig.

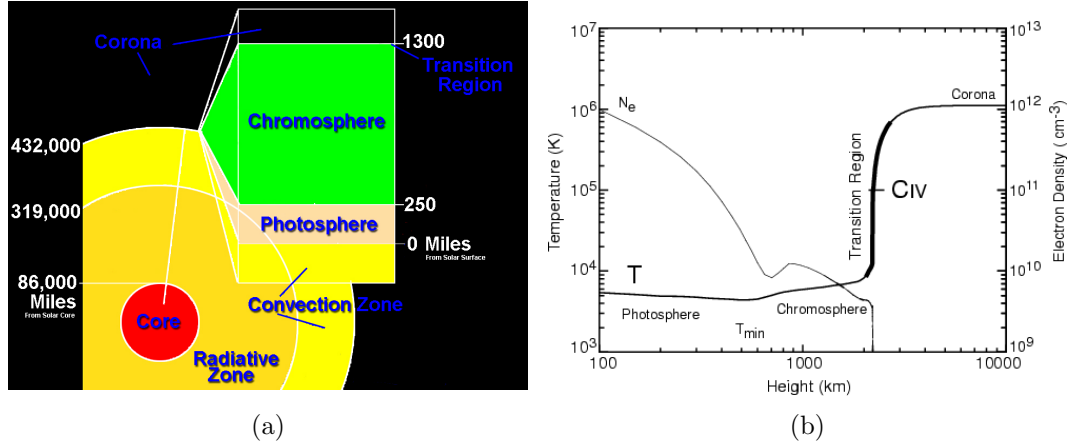


Figure 1.2 : (a) Schematic showing the layers of the solar atmosphere; the corona is the uppermost layer of the atmosphere. Courtesy of NASA (b) Temperature and density as a function of height above the solar surface; the corona is characterized by low densities and anomalously-high temperatures. Taken from Gary et al. (2007)

1.1), the corona is highly-structured and diffuse. Here, the temperature continues to increase, with typical coronal temperatures exceeding 1×10^6 K. Particularly high temperatures ($\approx 1 \times 10^7$ K) have also been observed in *active regions*, sites of intense magnetic activity associated with sunspots. These active regions can contain plasma as cool as 1×10^4 K as well and represent some of the most dynamic portions of the solar corona.

The work presented here will focus primarily on the plasma dynamics in the corona, in particular, in the cores of active regions where the intense magnetic field drives the motion of the plasma. In the following sections, we will discuss the origin of the solar magnetic field, its topology, how it impacts plasma in the solar corona, and finally how it connects to the anomalously high temperatures seen in the upper solar atmosphere.

1.2 The Solar Magnetic Field

Because of the high temperatures that characterize both the solar atmosphere and interior, much of the gas that makes up the Sun is ionized; that is, each atom has been stripped of at least one of its electrons. This means that the Sun is filled by a sea of charged particles, or plasma. In the corona where temperatures are often higher than 1×10^6 K, even heavy elements such as Mg, Ca, and Fe are stripped of their electrons. Because these particles are charged, their motion is strongly dictated by both the electric and magnetic fields via the Lorentz force law. Thus, to understand the dynamics of the coronal plasma, one must first try to understand the magnetic field that ultimately controls it.

1.2.1 The Solar Dynamo and Flux Emergence

The Sun, like the Earth, possesses an intrinsic magnetic field, though its origin and dynamics constitute a largely unsolved problem. Additionally, unlike Earth, the solar magnetic field is highly dynamic and comparatively quite strong (up to 1000 G in sunspots as compared to the < 1 G field on Earth) (Aschwanden, 2006). From the earliest studies of magnetism, it has been known that a conductor moving through a magnetic field produces a current. This current then in turn produces an additional magnetic field. Treating the convection zone (below the photosphere) plasma as the conductor and assuming some preexisting, but small magnetic field leads to what is commonly known as *dynamo theory* (Golub & Pasachoff, 2010).



Figure 1.3 : (a) Flux emergence from twisted and tangled field below the photosphere yields loop structures that stretch high into the solar atmosphere. Taken from Gold (1964). (b) The coronal magnetic field topology is extremely complex, making determinations of coronal plasma dynamics difficult. Shown here is a magnetic field extrapolation constructed from an optical magnetogram. An image from the TRACE satellite is superimposed to show the loop structures. Taken from Reale (2010).

Dynamo theory seeks to show self-consistently how the interaction between the Sun’s hot plasma and some small initial field leads to the observed complicated topologies and field strengths. Modeling such a system is no easy task as the interactions between the field and the plasma are highly non-linear, meaning solving the so-called “dynamo equations” requires a significant amount of computational effort. But how does this field affect the plasma dynamics of the corona? The solar magnetic field is said to be *frozen in* to the solar plasma; that is, the field moves with the plasma. Since the Sun is not solid, it undergoes *differential rotation*, meaning that different latitudes are spinning at different rates. Since the field follows the motion of the plasma, this causes the normally dipolar (north-south aligned) field to have an east-west component. This amplified and twisted field is then carried up to the photosphere by magnetic buoyancy, an idea first proposed by (Parker, 1955), resulting

in dipolar loop-like structures poking through the solar atmosphere (see Fig. 1.3(a)).

This phenomenon, commonly referred to as magnetic flux emergence, is by no means a solved problem and is a continuing topic of research (see Cheung & Isobe, 2014).

Finding out how the solar magnetic field is generated and how it makes its way to the upper atmosphere will undoubtedly help to explain much of the observed plasma dynamics in the corona.

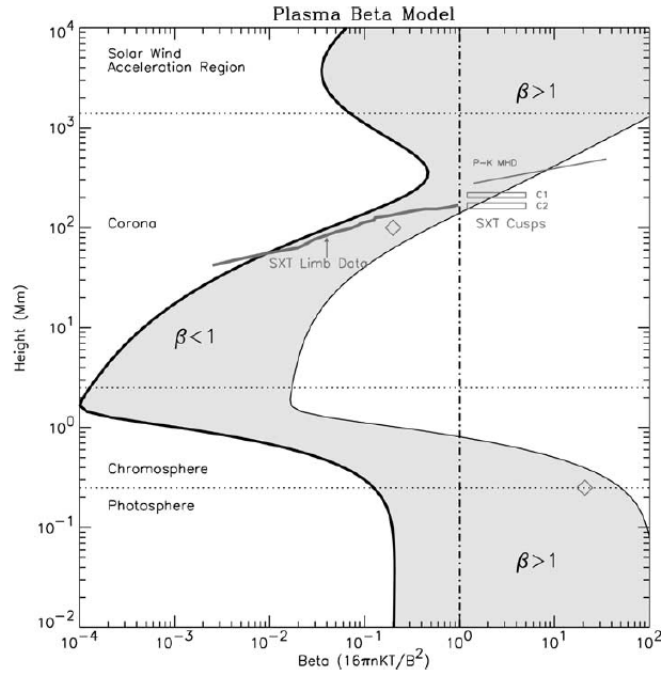


Figure 1.4 : Evolution of β as a function of height in the solar atmosphere. In the chromosphere, the gas pressure dominates ($\beta > 1$) while in the corona, the opposite is true and $\beta < 1$, making cross-field motion negligible. Out in the solar wind, the plasma returns to $\beta > 1$. Taken from Gary (2001).

1.2.2 Magnetic Reconnection

After the magnetic field is forced into the solar atmosphere by the buoyant motion of the convective zone, it remains rooted in the photosphere, whether it is an *open* (flux tube extends radially outward, possibly connecting with the interplanetary magnetic field) or *closed* (both ends attached to the solar surface) field line. Because the field is *line-tied*, or frozen into the photospheric plasma, the turbulent motion of the photosphere deforms and stresses the overlying field, leading to the storage of magnetic energy. This motion can eventually lead to a topological restructuring of the magnetic field as it relaxes from a stressed to an equilibrium state, a process popularly known as *magnetic reconnection*.

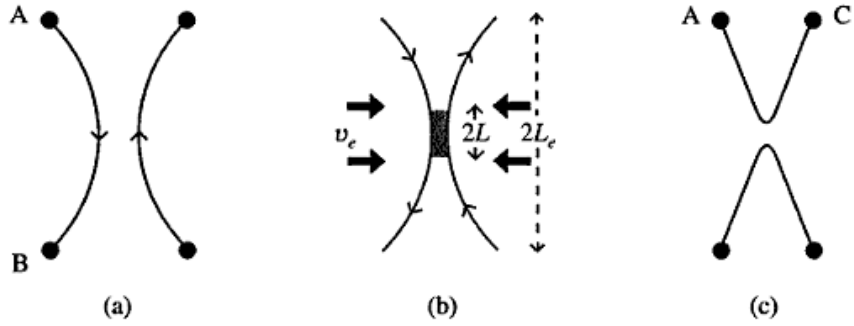


Figure 1.5 : Cartoon showing basics of reconnection process. Image taken from Priest & Forbes (2000).

Magnetic reconnection is thought to be a dominant process in a variety of space and astrophysical plasma environments, including Earth's magnetosphere, solar flares, and accretion disks. Additionally, reconnection has also been observed in laboratory settings such as the tokamak and the reversed field pinch (Priest & Forbes, 2000).

It is also thought to be the primary driver of some coronal heating mechanisms (see §1.3.2). The basic idea behind reconnection is illustrated in Fig. 1.5. When two oppositely-directed field lines are brought together in a conducting fluid (such as a plasma), a tangential discontinuity develops between them with current-carrying plasma squeezed into this area of discontinuity. Because the field lines are frozen into the plasma, a large magnetic gradient develops at the discontinuity in an area called the *diffusion region* (the gray box in Fig. 1.5). Because of these large gradients, the resistivity in this region becomes very high, allowing the magnetic field lines to diffuse through the plasma, reconnect, and relax to a topologically different, but more energetically favorable state. As the field lines reconnect and are pushed out of the diffusion region, they accelerate and heat the plasma. Reconnection is thus a non-ideal process as it allows for the conversion of stored magnetic energy to kinetic and thermal energy via dissipation (Priest & Forbes, 2000).

Research into magnetic reconnection has been continually driven by the desire to understand fundamental processes in astrophysical plasmas, primarily those that heat the corona and lead to solar flares. The first complete theory of reconnection was proposed by Sweet (1958) and Parker (1957, 1963). In the Sweet-Parker model, as it is popularly known, a diffusion region of length $2L$ and width 2ℓ is defined between two anti-parallel fields. The field lines are carried into the diffusion region with speed $v_i = \eta/\ell$, where η is the magnetic diffusivity. Using Maxwell's equations and the mass and momentum conservation equations from magnetohydrodynamic (MHD) theory,

the inflow velocity, or reconnection rate, can be rewritten as $v_i = v_{Ai}/\sqrt{R_{mi}}$, where v_{Ai} is the Alfvén speed and $R_{mi} = Lv_{Ai}/\eta$ is the Magnetic Reynolds number (Priest & Forbes, 2000). Unfortunately, the Sweet-Parker model predicts a reconnection rate far too slow to properly account for the energy release timescales observed in flare plasmas. In an effort to remedy the slow reconnection in the Sweet-Parker mechanism, Petschek (1964) suggested that magnetoacoustic shocks could provide an additional acceleration mechanism for the reconnection rate. Additionally, he proposed a smaller diffusion region, further shortening the reconnection timescale. For many years following Petschek’s work, it was thought that the problem of fast reconnection was solved. Today, however, thanks in part to increased computing power that makes three-dimensional and kinetic simulations possible, reconnection is now understood to be a far more subtle mechanism than previously thought, with the Petschek and Sweet-Parker models as only special cases (Priest & Forbes, 2000).

It goes without saying that the solar magnetic field is an extremely complex and dynamic system. Fortunately, one can still gain insight into the solar corona without completely solving the problems of the solar dynamo or magnetic reconnection. The corona constitutes what is commonly referred to as a “low-beta plasma” such that $\beta = p_{\text{thermal}}/(B^2/8\pi)$, the ratio between the gas pressure and magnetic pressure, is $\beta < 1$ (see Fig. 1.4). This means that the coronal magnetic field acts as a guide for the plasma, with the flow directed primarily in the field direction with negligible cross-field motion. A useful analogy is that of water flowing through a pipe: the

rigid pipe directs the flow of the water, but has no affect on the underlying fluid dynamics. Provided the field is reasonably stable and the relevant fluid equations are parameterized in terms of the field-aligned coordinate, our equations governing the plasma dynamics need not include the field at all!

Talk about drawbacks, mention MHD and hydrodynamic and hydrostatic; lead into coronal heating conversation; not sure if this is actually needed here...

1.3 The Coronal Heating Problem

Thus, far we have not addressed the important question of why the solar corona is so much hotter than the surface. From an intuitive, thermodynamic perspective, we would expect the atmospheric temperature to decrease as we moved away from the surface. However, nearly 70 years of observations have shown this is not the case and these anomalously high temperatures, dubbed the “coronal heating problem,” continue to baffle solar physicists today.

The discovery of the $> 1 \times 10^6$ K corona was made over the course of nearly fifty years through many laborious spectroscopic observations. Spectroscopic measurements during the late-nineteenth and early twentieth centuries of solar eclipses and images obtained from coronagraphs yielded a surprising result: an unknown line at 5303 Å , dubbed the “coronal green line” (Golub & Pasachoff, 2010). Because the line could not be associated with any known element, the line was identified as a new element, “coronium”. Later, more detailed examinations of the coronal spectrum re-

vealed several more unidentifiable spectral lines. Grotrian (1939) showed that many of these lines were due to highly ionized states of heavy elements such as iron and calcium. Additionally, Edlén (1943) identified four additional coronal lines, Fe X, Fe XI, Ca XII, and Ca XIII, providing more evidence for the presence of highly-ionized atoms in the corona and implying temperatures in excess of 1×10^6 K. Because of their work in coronal spectroscopy, Grotrian (1939) and Edlén (1943) are generally credited with the discovery of the million-degree solar corona. However, some (see Peter & Dwivedi, 2014) have argued that early coronal spectroscopists did not imply a million-degree corona and that it was in fact Nobel laureate Hannes Alfvén, in Alfvén (1941), who first proposed a hot corona, even arguing that it was the interaction between the magnetic field and the charged particles in the solar atmosphere that thwarted our usual thermodynamic intuition.

While these early spectroscopic observations are now better understood and a multitude of satellite observations have allowed a much clearer picture of the solar atmosphere, the exact mechanism responsible for the million-degree corona remains unknown. This is certainly not for lack of effort; over the last several decades, many different heating mechanisms have been proposed. These are traditionally divided into two-separate categories: *AC*, mechanisms that rely on waves to transfer energy from the lower atmosphere into the corona and *DC*, mechanisms that involve dissipation of energy stored in the stressed magnetic field. In order to be successful, a given mechanism must be able to explain the energy source of the heating, how the energy

is converted to heat, how the plasma responds and accurately predict any observables from the resulting plasma emission (see Fig. 1 in Klimchuk, 2006).

1.3.1 AC Heating

The same turbulent sub-photospheric motions that stress the magnetic field can also generate waves capable of propagating into the upper solar atmosphere. The AC- or DC-type heating classification depends on the timescale of the stressing motion: if it is longer than a characteristic crossing time of the coronal structure, it is classified as DC heating. If the timescale is shorter than a crossing time, it is classified as AC heating. A variety of wave modes have been observed in both the open and closed corona, including acoustic waves, Alfvén waves, and slow- and fast-mode MHD waves (Aschwanden, 2006). However, the simple existence of these waves is not enough to make them a viable candidate for coronal heating; they must be able to propagate into the corona with an adequate amount of energy and then efficiently dissipate this energy in order to heat the coronal plasma. For example, acoustic waves are capable of carrying an adequate amount of energy to heat the corona, but are almost entirely reflected by the steep density gradients in the transition region. Alfvén waves may also be capable of carrying enough energy to heat the corona, but specific frequencies are required to avoid reflection at the transition region. These particular modes have also been found to be non-dissipative under coronal conditions, making it hard for these waves to actually heat the corona even if they make it to the upper atmosphere

(Klimchuk, 2006). Wave modes generated in the corona would of course overcome the problem of crossing the transition region boundary. However, while oscillations in the corona have been observed (De Moortel et al., 2002b,a), the properties of these waves have not been measured precisely enough to say whether or not they are capable of heating the corona (Klimchuk, 2006).

1.3.2 DC Heating

As discussed in §1.2, the magnetic field that extends into the corona is rooted in the photosphere. Because of the underlying convection zone, the footpoints of these magnetic loops are subject to a turbulent velocity field and thus undergo a random walk across the surface. The turbulent motion of the footpoints causes the overlying loops to become twisted and braided around each other, leading to a highly stressed magnetic field above the solar surface. Gold (1964) first proposed the idea of a twisted field created by photospheric footpoint motions, suggesting that it was the relaxation of the stressed field to its equilibrium (or force-free) state that provided the energy release mechanism needed to power flares. Parker (1983a,b) applied this same concept to the corona and showed analytically that closely-packed magnetic flux tubes are subject to “dynamical nonequilibrium and reconnection” and that such a configuration easily leads to braided and twisted field lines with enough free energy to power the corona. Fig. 1.6(a) shows a cartoon of Parker’s braided field lines.

While Gold (1964); Parker (1983a,b) included few comparisons to observations

(mainly due to the lack of high-resolution instruments of the day), observations from the recently-launched High Resolution Coronal Imager (*Hi-C*) seem to support the idea of magnetic braiding. Cirtain et al. (2013) report two observations, in particular, from the *Hi-C* instrument that show braided magnetic fields, supporting the idea of a DC heating mechanism. Something here about Hi-C resolution maybe

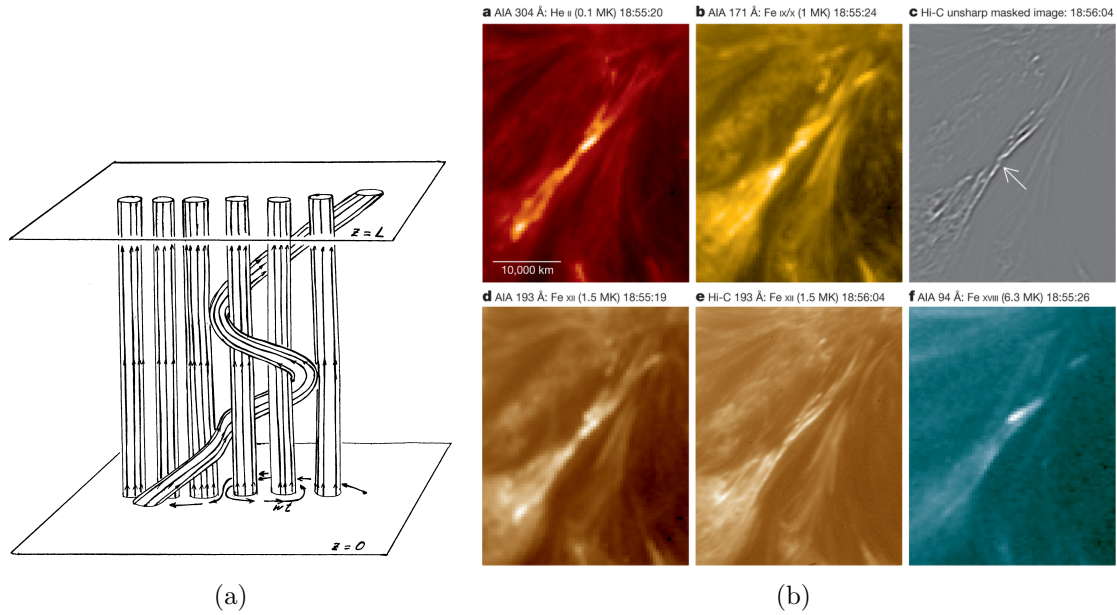


Figure 1.6 : (a) Cartoon showing braided flux tubes rooted, or line-tied, to the solar surface. Braiding allows for the build-up and relaxation of the field, providing an energy release mechanism capable of heating the solar corona. Taken from Parker (1983b). (b) Image from the *Hi-C* sounding rocket mission showing spatially-resolved braided flux tubes in the solar corona. Image taken from Cirtain et al. (2013).

This concept of braided and twisted fields illustrates the basic idea behind DC heating: energy is allowed to build up over time, most likely in the braided and twisted magnetic field as stressed by the turbulent footpoint motions, and then released, most likely through reconnection, as the field relaxes to a near-potential state. Parker

expanded on his early coronal heating theory with the now-seminal (Parker, 1988) in which he proposed that the 2-3 MK temperatures and 10^7 ergs cm^{-2} s^{-1} observed coronal energy input (Withbroe & Noyes, 1977) could be explained by many small, impulsive bursts of energy that he called *nanoflares*. These nanoflares are caused by the many tangential discontinuities that arise in the complex coronal magnetic field, leading to magnetic reconnection and the subsequent dissipation of the mechanical energy stored in the field by the random footpoint motions.

For the field, B , to become twisted and braided, the footpoints of the loop must have some transverse (with respect to the opposite footpoint, see Fig. 1.6(a)) velocity, v and thus a transverse field component, B_\perp . It can be shown that the work done on the field, W , by the footpoint motion is $W \propto v B_\perp B$, such that for $v = 0.5 \text{ km S}^{-1}$ and $B = 10^2 \text{ G}$, $W \approx 10^7 \text{ ergs cm}^{-2} \text{ s}^{-1}$, the observed value, when $\theta = \arctan B_\perp/B \approx 14^\circ$ (Parker, 1988). Using appropriate length scales, the energy per nanoflare event can be estimated as 10^{24} ergs, or about one-billionth of the energy of a typical flare. Thus, once $\theta = 14^\circ$, reconnection dissipates the stored energy and the field relaxes to equilibrium until it is wound up again by the footpoint motions, resulting in “bursty” energy release with the timescale and energy ultimately determined by the underlying velocity field and dissipation mechanism.

The Parker nanoflare concept has become one of the most favored and contentious coronal heating models (Cargill, 1994; Cargill & Klimchuk, 2004; Klimchuk, 2006). While many theoretical efforts (e.g. Bradshaw et al., 2012; Reep et al., 2013) have

shown the feasibility of nanoflares, the idea has long suffered from a lack observational evidence, though recent high-resolution and high-cadence observations (Brosius et al., 2014; Testa et al., 2013, 2014) have provided encouraging results. The term *nanoflare* has now become synonymous with impulsive heating in the energy range $10^{24} - 10^{27}$ ergs, with no specific assumption as to what underlying physical mechanism is responsible for this heating. Thus, in this work, the term nanoflare will refer to bursty energy release on a timescale of approximately 100 s or less.

1.4 Summary

The coronal heating problem is one of the most important unsolved problems in astrophysics. Gaining insight into the complex dynamics of the coronal magnetic field and plasma will allow us to better understand our own Sun and, in particular, how it affects our life here on Earth. Additionally, the field of solar physics has broader applications to fundamental astrophysical processes as studying our closest star will give us a better understanding of how stars throughout the universe behave and evolve. This thesis will focus on the study of coronal heating through the use of hydrodynamic models in which the underlying magnetic field is assumed to be static. In particular, this work will analyze how different heating models affect the emission measure and the resulting observables. This approach, commonly referred to as *forward modeling*, allows one to assess the physical validity of a number of free parameters when compared to observations. §2 will discuss loop structures in the

solar corona with an emphasis on recent observational findings and current modeling techniques. §3 will detail the emission measure diagnostics commonly used in coronal loop physics; in particular, how the line intensities are interpreted and how the differential emission measure (DEM) and other observables are inferred from observations. The details of the efficient hydrodynamic model used in this work will be discussed in §4, with particular emphasis given to the improvements made upon previous models. Finally, §5 and §6 will include the results and conclusions of our study, respectively, with comments regarding future work and improvements included in the latter.

Chapter 2

Coronal Loops

This chapter will discuss the discrete nature of corona in terms of coronal loop structures; Need a section on general plasma dynamics of loops to discuss energy transfer/loss/gain through heating/enthalpy/radiation/draining/filling; Also discuss general structure and how they are formed ;Give some general characteristics about them like length, temperature, density, through what layers they extend etc.; Show nice schematic

As discussed in §1.2.1, magnetic field lines emerge from below the photosphere due to magnetic buoyancy and differential rotation, extending high into the atmosphere with their footpoints rooted in the solar surface. Those field lines that are closed (both footpoints line-tied) form arch-like structures called *coronal loops*, the primary building blocks of the highly structured solar corona (Reale, 2010). Because $\beta < 1$ in the corona (see Fig. 1.4), the plasma is strongly confined such that the flow is directed primarily along the field with negligible cross-field motion. Thus, the enormously complicated magnetic field provides the scaffolding for the coronal plasma. As a consequence of this confinement, loops are individually isolated, leading to the observed inhomogeneity seen in the corona (Reale, 2010). Fig. 2.1 shows several distinct loop structures, both on-disk and off-limb, as observed in the 171 Å channel

of SDO/AIA.

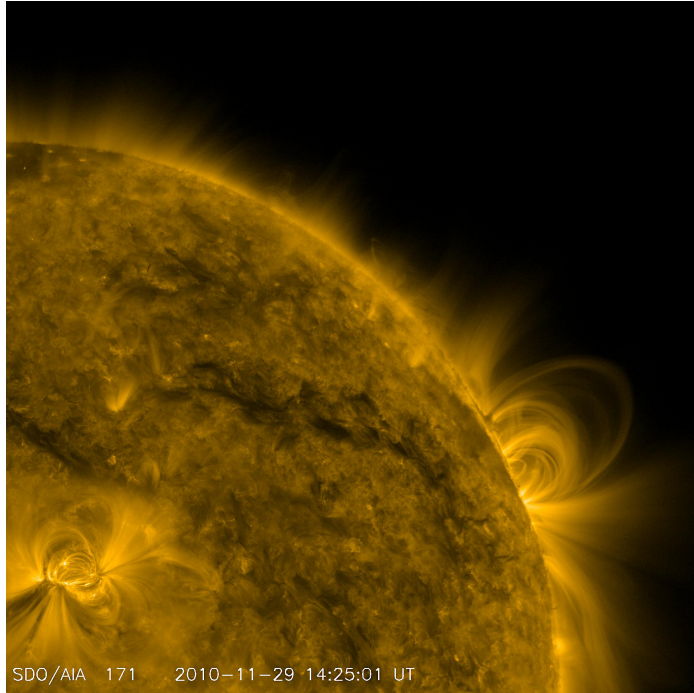


Figure 2.1 : Image captured by the 171 Å channel of the Atmospheric Imaging Assembly (AIA) onboard the Solar Dynamics Observatory (SDO). An arcade of loops in an active region can be seen on-disk in the lower left corner. Several prominent loop structures also appear off-limb on the right side. Image courtesy of NASA/SDO.

Coronal loops, because of their relatively high temperatures ($\sim 10^5 - 10^7$ K), are observed primarily in the extreme ultraviolet (EUV) and x-ray bands, with an associated wavelength range of $1 \sim 100$ Å . While most coronal loop temperatures exceed 10^5 K, loop plasma can span a range of temperatures and densities, due to both the complexity of the underlying field and the fact that individual loops are thermally isolated. As a result, loops are often categorized based on their thermal properties: *cool*, 0.1-1 MK, *warm*, 1-1.5 MK, and *hot*, ≥ 2 MK (Reale, 2010). Whether these thermal categories actually represent distinct classes of loops or if they are all

just transient states of the same type of loop is an open question in the coronal loops community, with the main debate revolving around whether different physical processes are at work in each type of loop. Additionally, loops have also been observed in several topologically different features on the Sun. See Table 2.1 for some typical parameters associated with these distinct regions. This work will focus primarily on simulating loops in active regions, where many hot, nonflaring loops have been observed and emission from loop plasma is unlikely to be contaminated by radiation from the underlying transition region (Tripathi et al., 2011; Warren et al., 2011, 2012; Winebarger et al., 2011).

Table 2.1 : Typical parameters for several different types of loops. Adapted from Reale (2010).

Region	L [10 ⁹ cm]	T [10 ⁶ K]	n [10 ⁹ cm ⁻³]
Bright points	0.1-1	2	5
Active regions	1-10	3	1-10
Giant arches	10-100	1-2	0.1-1
Flaring loops	1-10	> 10	> 50

2.1 Observations

Discuss some observations of loops and what has been learned about them, what constraints, multi-stranded versus single stranded Show some pretty pictures; if coronal loops are heated by nanoflares, what would be the observational signature?

The first evidence of magnetically confined loop structures came from soft x-ray observations by grazing-incidence telescopes aboard rocket missions in the late 1960s as reported by Vaiana et al. (1968). Analysis of data from these early missions

also allowed for classification of distinct topological features on the solar surface by Vaiana et al. (1973) (see Table 2.1). These early findings provided the first look at the x-ray-bright, highly-structured corona; however, the short observing times of these rocket missions prevented systematic studies of these newly-discovered structures. The first sustained coronal loop observations did not come until the Orbiting Solar Observatory IV, equipped with a grazing-incidence x-ray telescope, and the x-ray telescope aboard the *Skylab* space station (Krieger et al., 1972; Reale, 2010). Long observing times allowed for more accurate determinations of loop lifetimes, better comparisons between observations and loop models, and, perhaps most importantly, the finding that the coronal loop is the essential building block of all coronal structures (Rosner et al., 1978).

Need to introduce heating properties, frequency as the parameter we are most concerned about, review arguments for steady versus impulsive heating

In order to make accurate determinations regarding the physical processes and properties of coronal loops, large statistical surveys are needed. However, isolating and analyzing individual loops is incredibly difficult, due primarily to inadequate instrument resolution relative to coronal length scales. In general, loop structures resolved by current observing instruments are considered to be *multi-stranded*; that is, they are composed of many sub-resolution *strands*, where a strand is the smallest loop for which the cross-section is isothermal (Bradshaw et al., 2012). Need something here about active region cores specifically and why we choose to study these

over other parts of the AR

2.2 Modeling

While observations of increased spatial and temporal resolution are and will continue to be critical to gaining a better understanding Discuss modeling approaches, hydrodynamics versus magnetohydrodynamics, etc.

2.2.1 Static versus Dynamic

arguments for both; hydrostatic solutions briefly; scaling laws maybe combine MHD and hydrodynamics into single section, briefly mentioning MHD and why we discard the field

2.2.2 Magnetohydrodynamics

2.2.3 Hydrodynamics

2.3 Summary

Chapter 3

Emission Diagnostics

In solar physics (and astrophysics in general), all observational data must be collected through *remote sensing* techniques rather than *in situ* measurements due to the great distances and extreme environments inherent to the discipline. This means that atomic data and spectroscopy must be used to infer properties about the coronal plasma, including the temperature and density. To a good approximation, the hot, tenuous coronal plasma is *optically thin* to radiation emitted in the visible, ultraviolet (UV), and x-ray bands. This means that, between the observer and where the radiation was produced, the photons were not scattered or absorbed and reemitted. As a result, the observed radiation contains signatures of the plasma that produced it and has not been polluted by some intermediate process.

3.1 Spectral Line Intensity

As discussed in §1.3, spectroscopy has been a critically important tool in solar physics since the discovery of the million-degree corona. Modern observing instruments and techniques have allowed for the collection of an unprecedented amount of data at increasingly higher spatial resolution and temporal cadence. However, interpreting this spectroscopic data in terms of useful plasma parameters (e.g. density

and temperature) continues to pose a challenge to both observers and modelers alike.

The dominant emission mechanism in the high-temperature, low-density solar corona is *bound-bound* emission,



where X represents the atomic species, m is the charge state, h is Planck's constant, and $\nu_{j,i}$ is the frequency of the emitted photon of energy $\Delta E_{j,i} = h\nu_{j,i} = hc/\lambda_{j,i}$, with j and i representing the bound and lower energy states, respectively (Mason & Fossi, 1994). In this process, ion X^{+m} spontaneously decays from excited state j to lower-energy state i , emitting a photon of frequency $\Delta E_{j,i}$. The associated emissivity (power per unit volume) for the transition can then be written as

$$P(\lambda_{j,i}) = N_j(X^{+m})A_{j,i}\Delta E_{j,i}, \quad (3.2)$$

where $N_j(X^{+m})$ is the number density of element X with charge state $+m$ in excited state j and $A_{j,i}$ is the Einstein spontaneous emission coefficient. Thus, the power for a given spectral line is dependent on both the number of ions of a particular charge state and the number of ions in that particular charge state who are also in an excited state (Mason & Fossi, 1994; Bradshaw & Raymond, 2013). Finally, this volumetric

power can be related to the observed line intensity as at Earth,

$$I(\lambda_{j,i}) = \frac{1}{4\pi R^2} \int_V dV P(\lambda_{j,i}), \quad (3.3)$$

where the integral is taken over the entire sphere of radius R , where R is the distance to the observer, and then normalized by the surface area of the sphere.

The next question is of course how these measured line intensities can be related to the properties of the coronal plasma. In Eq. 3.2, $A_{j,i}$ can be calculated from laboratory experiments for a given transition and $\Delta E_{j,i}$ is easily found provided $\lambda_{j,i}$ is known. The remaining quantity, $N_j(X^{+m})$ can be expressed as a series of ratios,

$$N_j(X^{+m}) = \frac{N_j(X^{+m})}{N(X^{+m})} \frac{N(X^{+m})}{N(X)} \frac{N(X)}{N(H)} \frac{N(H)}{N_e} N_e, \quad (3.4)$$

where $N(X^{+m})$ is the number density of element X in charge state $+m$, $N(X)$ is the number density of element X , $N(H)$ is the number density of hydrogen, and N_e is the electron number density (Mason & Fossi, 1994). Note that $N_j(X^{+m})$ has just been repeatedly multiplied by one in order to reexpress it in terms of the following ratios (from left to right in Eq. 3.4): fraction of $+m$ -ions in excited state j , fraction of X atoms in charge state $+m$, relative abundance of X compared to hydrogen, and relative abundance of hydrogen compared to the number of electrons. The expression can be further simplified through the definition of the relative abundance $Ab_X = N(X)/N(H)$ and the common approximation $N(H)/N_e \approx 0.83$.

Eq. 3.2, and thus Eq. 3.3, can be further simplified by invoking the *coronal model* approximation. In optically-thin plasmas, it can be assumed that the collisional excitation and radiative decay occur from and to the ground state, respectively; in other words $i \rightarrow g$, with g representing the ground state. Additionally, the processes which determine the excitation level and those that determine the charge state are assumed to operate on disparate enough timescales such that the changes in energy level populations of the emitting ions, occurring on short timescales, can be decoupled from the changes in the charge state, occurring on longer timescales (Bradshaw & Raymond, 2013). Using these assumptions, statistical equilibrium between the spontaneous decay and collisional excitation processes demands

$$N_g(X^{+m})N_eC_{g,j}^e = N_j(X^{+m})A_{j,g}, \quad (3.5)$$

where $C_{g,j}^e$ is the electron collisional excitation rate between g and j (Bradshaw & Raymond, 2013). Plugging Eqs. 3.5 and 3.4 into Eq. 3.2 and letting $N_g(X^{+m}) \approx N(X^{+m})$ yields

$$P(\lambda_{j,g}) = (0.83)\text{Ab}_X\Delta E_{j,g}\frac{N(X^{+m})}{N(X)}C_{j,g}^eN_e^2. \quad (3.6)$$

Defining the *contribution function* $G(T, \lambda_{j,g}) = N(X^{+m})/N(X)C_{j,g}^e$, the intensity integral can be rewritten as

$$I(\lambda_{j,g}) = \frac{(0.83)\text{Ab}_X\Delta E_{j,g}}{4\pi R^2} \int_V dV N_e^2 G(T, \lambda_{j,g}). \quad (3.7)$$

If the plasma is isothermal over the emitting volume V , $G(T, \lambda_{j,g})$ comes outside the integral such that

$$I(\lambda_{j,g}) = \frac{(0.83)\text{Ab}_X \Delta E_{j,g}}{4\pi R^2} G(T, \lambda_{j,g}) \langle \text{EM} \rangle, \quad (3.8)$$

where $\langle \text{EM} \rangle = \int_V dV N_e^2$ is the average *emission measure*. However, in many cases, this isothermal approximation does not hold such that the intensity integral must be expressed as

$$I(\lambda_{j,g}) = \frac{(0.83)\text{Ab}_X \Delta E_{j,g}}{4\pi R^2} \int_V dT \phi(T) G(T, \lambda_{j,g}), \quad (3.9)$$

where $\phi(T) = N_e^2 dV/dT$ is the *differential emission measure* (DEM).

3.2 Differential Emission Measure

The DEM and EM provide information about the temperature distribution of the plasma. In particular, the DEM is a measure of the amount of emitting material at a particular temperature T in the plasma. Thus, the DEM is an observable that any viable theory of coronal heating should be able to predict with reasonable accuracy (Golub & Pasachoff, 2010). Furthermore, because the DEM is a one-dimensional function, it provides a simple and powerful characterization of the multi-thermal coronal plasma. Unfortunately, calculating these quantities from observed line intensities is difficult because of both mathematical and data availability issues. Looking back to Eq. 3.8, one can see that, provided the line intensities and contribution functions

are available over a significant range of temperatures, the emission measure can be calculated algebraically.

3.2.1 Reconstruction Techniques

If the plasma is assumed to be approximately isothermal over the emitting volume, say at temperature T_C , the contribution function can be taken outside of the integral as in Eq. 3.8. Furthermore, if the plasma is assumed to have a constant density over the emitting volume as well, then $\langle \text{EM} \rangle \approx N_e^2 V$. To determine the T_C , the temperature of the plasma, the emission measure for each spectral line is calculated over the appropriate temperature range,

$$\langle \text{EM}(T) \rangle = 4\pi R^2 \frac{I_j}{(0.83)\text{Ab}_X \Delta E_j G_j(T, N_e)}, \quad (3.10)$$

where the contribution function G for a particular spectral line j at temperature T and density N_e can be calculated using the CHIANTI atomic database (Dere et al., 1997; Landi et al., 2013). Typically, this procedure is done for a sufficiently large sample of observed spectral line intensities and the corresponding $\langle \text{EM}(T) \rangle$ curves plotted on top of each other. Because of the isothermal assumption, these curves should intersect at a common point, $(T_C, \langle \text{EM}(T_C) \rangle)$ (Landi et al., 2002). Of course this isothermal condition is never actually met; thus, all curves tend to meet in a region of intersection. The more multithermal the plasma is, the broader the region of intersection will be and, consequentially, the value of T_C will be less constrained,

leading to indeterminate measurements of the plasma temperature. An example for a simulated data set with a very narrow temperature distribution and thus a well-determined value of T_C is shown in Fig. 3.1(a).

Relaxing the isothermal assumption introduces a great deal more complexity. Unlike $\langle \text{EM} \rangle$, $\phi(T)$ cannot be determined algebraically; instead, Eq. 3.9, a Fredholm equation of the first kind, must be inverted to find $\phi(T)$, a task that poses well-known mathematical difficulties (Kashyap & Drake, 1998). One method for performing such an inversion is a discretization of Eq. 3.9

$$I_j = \frac{(0.83)\text{Ab}_X\Delta E_j}{4\pi R^2} \sum_{k=1}^N \phi_k \int_{T_k}^{T_{k+1}} dT G_j(T), \quad (3.11)$$

where j labels the spectral line and $[T_{k+1}, T_k]$ is the temperature interval over which ϕ_k is constant. For each measured line intensity I_j , ϕ_k for $1 \leq k \leq N$ are determined through some minimization procedure (Landi et al., 2012). To calculate the DEM curve, an arbitrary spline or polynomial is first assumed; subsequent corrections at $T_{eff,j}$, the temperature of maximum abundance for the line intensity I_j , are then calculated and a spline interpolation applied to these corrections for the entire temperature range $[T_1, T_N]$. This correction is then applied to initial curve and the corrected curve is used as the initial DEM on the next iteration (Landi et al., 2012). This method of course has the disadvantage that a functional form for the DEM must be chosen *a priori*, biasing the temperature distribution. Additionally, a poor choice of temperature interval in Eq. 3.11 can oversmooth the DEM curve or cause

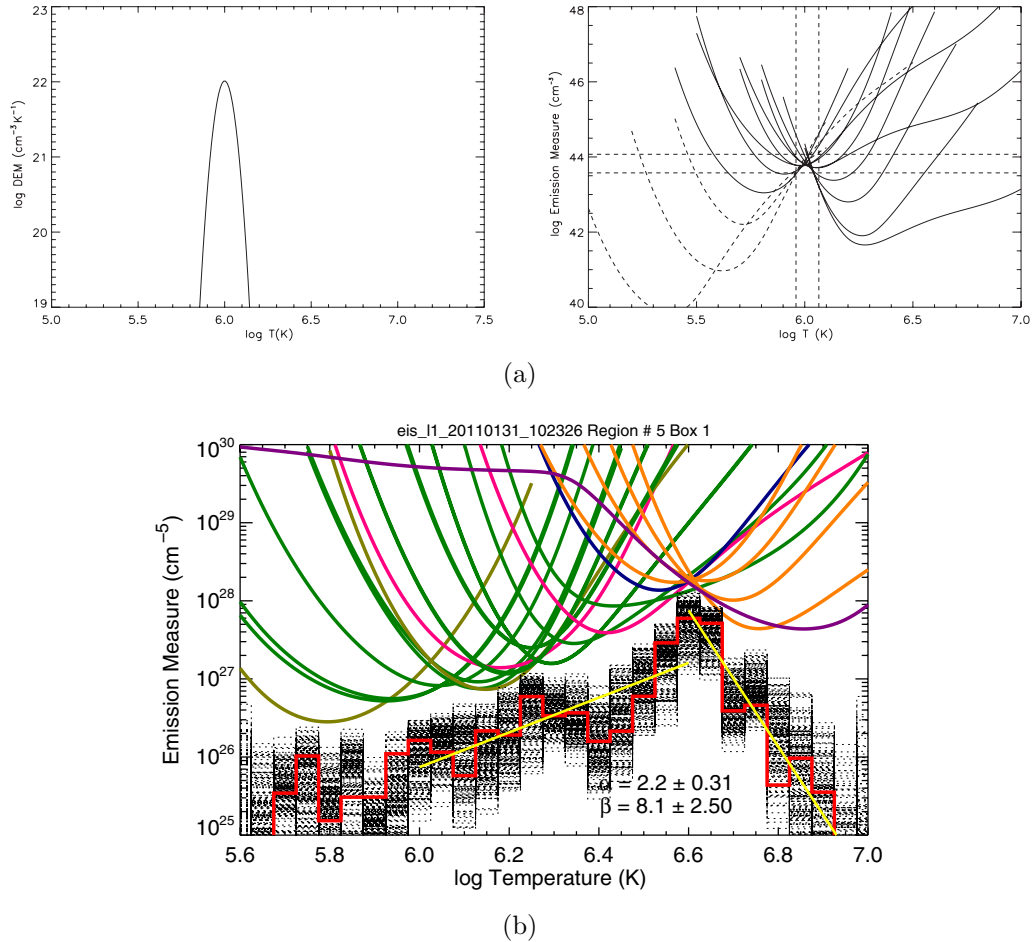


Figure 3.1 : (a) Simulated DEM curve and the resulting EM loci reconstruction. From the DEM curve, the plasma is approximately isothermal, being sharply peaked about 1 MK. Correspondingly, the EM loci curves intersect in a region centered on 1 MK, allowing for a well-constrained determination of T_C . Image taken from Landi & Klimchuk (2010). (b) Emission measure distribution reconstruction for an active region core. The colored curves show the emission measure calculation using the EM loci method. The black and red histograms show the $\text{DEM}(T)dT$ reconstructed using the MCMC method of Kashyap & Drake (1998). Here, the DEM is multiplied by the temperature bin for comparison with the EM loci calculation. The yellow lines to the left and right of the peak show the cool and hot slope fits in the ranges $6.0 < \log T < 6.6$ and $6.6 < \log T < 7.0$, respectively. Image taken from Warren et al. (2012)

convergence issues.

An alternative method for calculating the DEM that has begun to gain popularity is the Markov-chain Monte Carlo (MCMC) method developed by Kashyap & Drake (1998). Using a Bayesian approach, the goal of this method is to maximize the probability $P(X, F)$ of obtaining observed line intensities $F = (F_1, F_2, \dots, F_n)$ from a DEM characterized by a set of parameters $X = (X_1, X_2, \dots, X_m)$. First, a set of N temperature bins is chosen such that within each bin, the plasma is assumed to be isothermal and can be described by an emission measure EM_i . As a result, the set of parameters X that describe the DEM is $X = (\text{EM}_1, \text{EM}_2, \dots, \text{EM}_N)$. To maximize $P(X, F)$, the parameters of X are varied step by step such that the change introduced only depends on the parameters of the previous step. This new set of parameters X' has a new probability $P(X', F)$ and this new set of parameters is accepted or rejected based on the Metropolis algorithm (Metropolis et al., 1953). The emission measure values in each bin thus comprise the DEM. Unlike other reconstruction methods, the MCMC method has the benefit of not assuming *a priori* a functional form for the DEM curve and does not impose unphysical smoothness constraints on the final solution (Landi et al., 2012).

3.2.2 Scaling Laws

From these emission measure distributions, simple observables can be calculated that any viable heating model should be able to produce. The most popular of

these observables is the well-known scaling between the emission measure and the temperature,

$$\text{EM} \propto T^a. \quad (3.12)$$

This scaling, first proposed by Jordan (1980), has since been validated by both simulation and observation. A summary of model and observational results for the a parameter can be found in Table 3.1. Looking at the sample emission measure distributions in Fig. 3.1, it can be seen that, for isothermal (Fig. 3.1(a)) and multithermal (Fig. 3.1(b)) plasmas, the emission measure distribution tends to be strongly peaked. When determining the scaling parameter a , it is common perform a linear fit in $(\log T, \log \text{EM})$ coolward of the peak, typically between 6.0 and $\log T_{peak}$, where T_{peak} is the temperature at which EM_{max} occurs. Observations of the inter-moss regions of active region cores, where the emission is less likely to be contaminated by transition region lines, indicate that $2 \lesssim a \lesssim 5$. Table 3.1 summarizes these findings. This large range of values is most likely due to both uncertainties in the atomic data as well as the variety of techniques used to reconstruct the emission measure distribution (see §3.2.1).

These scalings have also recently been studied in the context of simulation. Mulu-Moore et al. (2011), using a 1D hydrodynamic model, constructed emission measure distributions for a 3×3 parameter space of loop length and equilibrium temperature using a single impulsive heating function. They found that this “long nanoflare storm” heating scenario, in which impulsive heating events occur infrequently on

sub-resolution strands, produced emission measure slopes that were too small to adequately account for observations. Using an advanced forward modeling technique and a different 1D hydrodynamic model, Bradshaw et al. (2012) and Reep et al. (2013) investigated the effect of low-frequency and high-frequency nanoflare heating, respectively, on the resulting emission measure. Bradshaw et al. (2012) found that low-frequency heating could not account for the entire range of observed emission measure slopes while Reep et al. (2013) showed high-frequency heating could. Additionally, Cargill (2014), using an efficient “0D” hydrodynamic simulation (see §4.2), showed that a can vary from 2 to greater than 5 depending on the heating frequency, whether the heating spectrum follows a power-law, and how the heating scales with the time between successive heating events.

As discussed in §1.3.2, nanoflares, short heating events on the order of 10^{24} ergs, are a plausible explanation for observed million-degree coronal temperatures. One strategy for testing and constraining this theory is to analyze modeled and observed emission measure distributions for signatures of impulsive heating. As with the cool emission, the hot emission is also often characterized by an emission measure slope. Typically, this linear fit on $\log T, \log EM$ is done “hotward” of the peak, usually in the range $6.0 \lesssim \log T \lesssim 7.2$. However, measured values of these hotward slopes are poorly constrained due to both the magnitude of emission and the lack of available spectroscopic data in this temperature range. Warren et al. (2012), using spectral measurements from *Hinode*/EIS, provided hotward fits for EM reconstructions for a

Table 3.1 : Summary of emission measure scalings from observational and modeling studies. Scalings are typically calculated coolward of the emission measure peak and typically range from 2 to 5. Adapted from Bradshaw et al. (2012).

Slopes, a	Range of $\log T$	Type	Reference
3.26	6.00-6.60	observation	Warren et al. (2011)
2.17		model	
3.20	6.00-6.50	observation	Winebarger et al. (2011)
2.08-2.47 (background)	5.50-6.55	observation	Tripathi et al. (2011)
2.05-2.70 (background subtracted)			
1.60-2.00 (photospheric abundances)	6.00-[6.60-6.80]	model	Mulu-Moore et al. (2011)
2.00-2.30 (coronal abundances)			
1.70-4.50	6.00-6.60	observation	Warren et al. (2012)
1.91-5.17	6.00-[6.30,6.80]	observation	Schmelz & Pathak (2012)
0.58-2.24 (low-frequency nanoflares)	6.00- $\log T_{peak}$	model	Bradshaw et al. (2012)
0.79-3.65 (nanoflare trains)	6.00- $\log T_{peak}$	model	Reep et al. (2013)
$\sim 2 - \sim 7$ (low- to high-frequency heating)	[6.00-6.25]- $\log T_{peak}$	model	Cargill (2014)

large number of active regions. All measured slopes fell in the range $6.1 < |a_{hot}| < 10.3$, with large uncertainties on each hotward fit. Examples of both a hotward and coolward fit on a reconstructed EM are shown in Fig.

3.2.3 Observational Difficulties

Cargill (1994); Cargill & Klimchuk (2004) have predicted that emission measure distributions resulting from nanoflare models should be wide and have a faint, high-temperature ($> 4 \times 10^6$ K) component and thus a steep hotward slope. Unfortunately, observing this high-temperature emission is difficult and in some cases impossible. The reason for this difficulty is twofold. First, thermal conduction is a very efficient cooling mechanism at high temperatures and large spatial temperature gradients. Thus, because the increase in density lags the increase in temperature due to heating and because $EM \propto n^2$, by the time sufficient densities are achieved, the plasma has cooled down such that the fingerprints of nanoflare heating have been smoothed out.

The second reason for this difficulty is non-equilibrium ionization. It is usually assumed that the observed line intensities, because of their known formation temperatures, are a direct indicator of the plasma temperature. However, if the heating timescale is shorter than the ionization timescale, the time it takes for the ion population to settle into the correct charge state, an equilibrium assumption can lead to a misdiagnosis of the plasma temperature. This makes signatures of hot, nanoflare-heated plasma especially difficult to detect if the high temperatures persist for less

than the ionization timescale (Bradshaw & Cargill, 2006; Bradshaw & Klimchuk, 2011; Reale & Orlando, 2008).

Despite these difficulties, various attempts have been made to observe this faint high-temperature emission, the so-called “smoking gun” of coronal nanoflares. Using the broadband X-Ray Telescope (XRT) aboard the *Hinode* spacecraft, Schmelz et al. (2009) and Reale et al. (2009) show a faint hot component in the reconstructed DEM curves. However, since the channels on such broadband instruments can often be polluted by low-temperature emission, the reliability of such measurements depends on the filtering technique used. Additionally, Winebarger et al. (2012) showed that combinations of *Hinode*/EIS and *Hinode*/XRT measurements leave a “blind spot” in the EM – T space coincident with where evidence for nanoflare heating is likely to be found. Unambiguous observational evidence of nanoflare heating must come from pure spectroscopic measurements (see Brosius et al., 2014). Missions like the Marshall Grazing Incidence X-ray Spectrometer (MaGIXS) (Kobayashi et al., 2011; Winebarger, 2014), with a wavelength range of 6-24 Å and a temperature range of $6.2 < \log T < 7.2$, aim to probe this previously poorly-resolved portion of the coronal spectrum in hopes of better quantifying the presence of faint, high-temperature plasma.

3.3 Forward Modeling

As discussed in §3.1 and §3.2, interpreting observational results involves many assumptions and can potentially lead to misleading physical conclusions. Forward modeling, the calculation of observables from simulations, helps to cut out many of the assumptions often used when converting results from a particular instrument to interpretable observations. These simulated observables can then be directly compared to real observations. Additionally, forward modeling is also useful in the design of new instrumentation. If an instrument is being designed to observe a specific phenomenon (e.g. nanoflare heating), it should be designed such that its sensitivity corresponds to the regime in which such a phenomenon can be observed. Forward modeling techniques can be used to simulate the specific physical event and then map the results to the specified detector geometry in order to determine what equipment is necessary in order to capture a signal from the specified event.

Because of the wealth of data available to solar physicists, forward modeling is an invaluable tool, particularly in the study of coronal heating. For example, in an effort to diagnose what signal AIA/SDO would observe, given an impulsive heating event in an active region, Bradshaw & Klimchuk (2011) used the HYDRAD model (Bradshaw & Cargill, 2013) to calculate temperature and density profiles as a function of time and loop coordinate, $T(s, t)$ and $n(s, t)$ for a variety of loop lengths, event durations and event amplitudes. These T and n values are then mapped from the loop geometry to the detector geometry as shown in Fig. 3.2(a). The observed intensity as a function

of s and t in units of data numbers per pixel per second can then be calculated as

$$\mathcal{I}(\lambda, n, T) = \frac{(0.83) \times \text{IR}(\lambda) \times \text{Ab}_X \times X_i \times \epsilon(\lambda, n, T) \times (\text{EM}_{pix}/A_{pix})}{4\pi \times (hc/\lambda)}, \quad (3.13)$$

where $\text{IR}(\lambda)$ is the instrument response function, X_i is the population fraction of charge state i of element X , ϵ is the emissivity of the line calculated using the CHI-ANTI atomic database and associated routines, EM_{pix} is the emission measure in the particular pixel, and A_{pix} is the area of the pixel (Bradshaw & Klimchuk, 2011).

When forward-modeling intensity in an impulsive heating scenario, X_i is one of the most critical quantites. Higher charge states are created through collisional ionization. The charge state varies strongly with the temperature and weakly with the density; at higher kinetic energies (i.e. temperatures), free electrons are capable of ionizing even inner, strongly-bound electrons leading to higher charge states while at low kinetic energies, electrons are more easily captured in the outer bound states, leading to lower charge states (Bradshaw & Raymond, 2013). The ionization state is determined by the equation

$$\frac{\partial X_i}{\partial t} + \frac{\partial(X_i v)}{\partial s} = n(I_{i-1}X_{i-1} + R_iY_{i+1} - I_iX_i - R_{i-1}Y_i), \quad (3.14)$$

where v is the bulk flow velocity and I_i and R_i are the ionization and recombination rates for charge state i , respectively. Setting the lefthand side to zero amounts to assuming equilibrium ionization. However, in an impulsive heating scenario, the

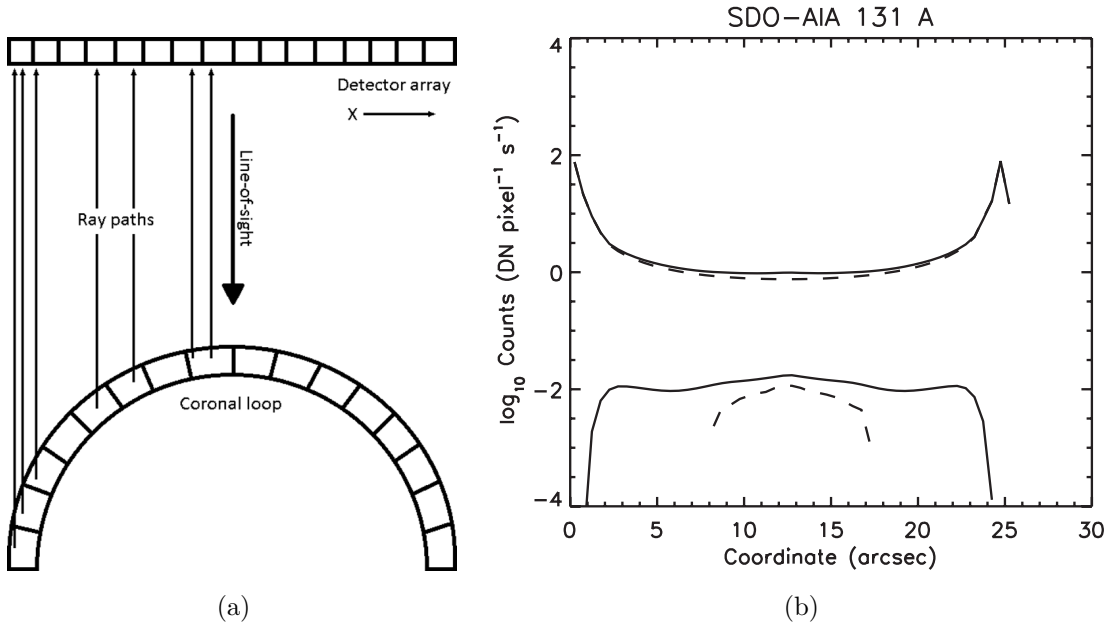


Figure 3.2 : (a) Diagram showing how the loop parameters are mapped to the detector geometry. More emission is concentrated at the ends of the detector array because of the curvature of the loop. (b) Plot of forward-modeled intensity as a function of loop coordinate as observed by the 131 Å channel of SDO/AIA. The upper and lower solid curves represent the total and hot-only emission assuming equilibrium ionization. The dashed curves correspond to non-equilibrium ionization. Both images taken from Bradshaw & Klimchuk (2011).

temperature changes so fast that there is a lag between the electron temperature and the temperature represented by spectral line emission. This is a consequence of the finite time that it takes for the ionization state to reach equilibrium. Solving Eq. 3.14 for a nonzero lefthand side allows one to properly take into account effects due to non-equilibrium ionization and thus correctly forward model emission from an impulsively-heated coronal loop. Fig. 3.2(b) shows how the assumption of ionization equilibrium can affect the observed intensity, especially in the case of hot plasma, one of the most important signatures of nanoflare heating.

This thesis will study the effect of differing loop and heating parameters, such as

event duration, amplitude distribution, and event frequency, on the resulting emission measure distribution. The emission measure will be calculated using the simple expression $\text{EMd}T = n^2 L$, where L is the loop length, rather than one of the reconstruction methods described in §3.2. In this way, the emission measure calculated here is the ground truth. In other word, effects due to observing or analysis techniques are not considered. Observables are then calculated by performing a linear fit on both the hotward and coolward slopes. Particular emphasis will be placed on the hotward slope calculations as few authors have concentrated on this portion of the emission measure distribution. Additionally, this portion of the plasma emission measure is also believed to characterize the properties of an impulsive coronal heating mechanism. Comparisons will be made to values reported in previous numerical studies and observational surveys.

Chapter 4

Numerical Modeling

Coronal loop modeling can be roughly divided into two categories: multi-dimensional (typically 3D) magnetohydrodynamic models and hydrodynamic models. The former focuses primarily on the study of the dynamics of the magnetic field itself; the latter concentrates on the response of the plasma for some *ad-hoc* heating and prescribed, static field geometry (Bradshaw & Cargill, 2013). While a hydrodynamic treatment may seem overly simplified, such models often provide a much more physically realizable treatment of the plasma than most 3D MHD models. This thesis will examine primarily the use of hydrodynamic models in the study of coronal plasma dynamics. By using hydrodynamic models, the evolution and response of the plasma to various heating functions can be carefully treated. In particular, this work will focus on the role of a two-fluid treatment in efficient hydrodynamic simulations. Such efficient models allow for the exploration of large parameter spaces with comparably little computational overhead.

4.1 One-dimensional Two-fluid Hydrodynamics

In §2.2.3, the hydrodynamic equations were discussed under the assumption that the electron and ion populations were in equilibrium at all times (i.e. a single-fluid

approximation). However, since the mechanism behind coronal heating is still highly debated, the degree to which the ions or electrons are preferentially heated is unknown. It is often assumed that the electrons are the direct recipients of the prescribed heating function. However, it is also possible that the ions are preferentially heated. One particular example is that of ion-cyclotron wave resonances (Markovskii & Hollweg, 2004). Ion cyclotron waves are excited by plasma instabilities in the lower corona. These waves then propagate upwards through the coronal plasma and wave particle interactions can occur for those ions whose gyrofrequencies have a resonance with the ion-cyclotron wave. Additionally, there is also evidence for ion heating via reconnection, both in laboratory plasmas and particle-in-cell simulations (Ono et al., 1996; Yoo et al., 2014; Drake & Swisdak, 2014). Thus, ion heating in the solar corona should not be discounted as a possibility.

In this work, quasi-neutrality, $n_e = n_i = n$, will be assumed. While the heavier ions are in higher charge states and have thus given up more than one electron per ion, $\text{Ab}_H \gg \text{Ab}_{X>H}$. In other words, the abundance of (singly ionized) H is so much greater than the multiply-ionized heavier elements that quasi-neutrality is a valid assumption. Additionally, current-free conditions are also assumed such that $v_e = v_i = v$. Under these assumptions, the conservative forms of the mass and

momentum equations can be written,

$$\frac{\partial \rho}{\partial t} = -\frac{\partial(\rho v)}{\partial s}, \quad (4.1)$$

$$\frac{\partial(\rho v)}{\partial t} = -\frac{\partial(\rho v^2)}{\partial s} - \frac{\partial(p_e + p_i)}{\partial s} + \frac{\partial}{\partial s} \left(\frac{4}{3} \mu_i \frac{\partial v}{\partial s} \right) + \rho g_{\parallel}, \quad (4.2)$$

where $\rho = m_e n_e + m_i n_i = n(m_e + m_i) \approx nm_i$, m_i is the ion mass, p_e and p_i are the electron and ion pressures respectively, and $\mu_i = m_i u_i$, where u_i is the classical Spitzer viscosity coefficient (Bradshaw & Cargill, 2013). Notice that Eq. 4.1 is equivalent to its single-fluid counterpart due to our assumption of quasi-neutrality and that the only difference between Eq. 4.2 and Eq. SF MOM EQ REF HERE is the addition of the ion viscosity term and that $p = p_e + p_i$.

The electron and ion energy equations are given by

$$\frac{\partial E_e}{\partial t} = -\frac{\partial}{\partial s}[(E_e + p_e)v] + v \frac{\partial p_e}{\partial s} - \frac{\partial F_e}{\partial s} + \frac{1}{\gamma - 1} k_B n \nu_{ei} (T_i - T_e) - E_R + E_{H,e}, \quad (4.3)$$

$$\frac{\partial E_i}{\partial t} = -\frac{\partial}{\partial s}[(E_i + p_i)v] - v \frac{\partial p_e}{\partial s} - \frac{\partial F_i}{\partial s} + \frac{1}{\gamma - 1} k_B n \nu_{ei} (T_e - T_i) + \frac{\partial}{\partial s} \left(\frac{4}{3} \mu_i v \frac{\partial v}{\partial s} \right) + \rho v g_{\parallel} + E_{H,i}, \quad (4.4)$$

where E_e and E_i are the electron and ion energies, respectively, and $E_{H,e}$ and $E_{H,i}$ are the *ad-hoc* volumetric heating rates for the electrons and ions, respectively. Fur-

thermore, this set of equations is subject to the closure conditions

$$E_e = \frac{p_e}{\gamma - 1}, \quad (4.5)$$

$$E_i = \frac{p_i}{\gamma - 1} + \frac{1}{2}\rho v^2, \quad (4.6)$$

$$p_e = k_B n T_e, \quad (4.7)$$

$$p_i = k_B n T_i, \quad (4.8)$$

where $\gamma = 5/3$ is the adiabatic index.

The conductive heat fluxes for the ions and electrons, F_e and F_i , are given by the classical Spitzer-Harm (Spitzer & Härn, 1953) formulas

$$F_e = -\kappa_{0,e} T_e^{5/2} \frac{\partial T_e}{\partial s}, \quad (4.9)$$

$$F_i = -\kappa_{0,i} T_i^{5/2} \frac{\partial T_i}{\partial s}, \quad (4.10)$$

where $\kappa_{0,e}$ and $\kappa_{0,i}$ are the Spitzer coefficients for electron and ion thermal conduction, respectively (Bradshaw & Cargill, 2013). The classical formula for the heat flux, however, is known to be inaccurate at high temperatures and low densities. To correct for this, a flux-limiter or free-streaming limit is often used, such that the heat flux saturates at

$$F_{sat,s} = -\beta \frac{3}{2} \frac{k^{3/2}}{m_s^{1/2}} n T_s^{3/2}, \quad (4.11)$$

where s specifies the particles species (Bradshaw & Cargill, 2006). This prevents the heat flux from becoming unphysically large, particularly during the onset of heating when the temperature is high and the density relatively low. β is a flux limiter constant with a typical value between 1 and 1/6 (Luciani et al., 1983; Karpen & DeVore, 1987). The final expression for the conductive flux for species s can then be written as

$$F_s = \frac{F_{c,s} F_{sat,s}}{\sqrt{F_{c,s}^2 + F_{sat,s}^2}}, \quad (4.12)$$

where $F_{c,s}$ is the classical expression for the heat flux for species s as given in Eqs. 4.9 and 4.10. Thus, $F_s \approx F_{c,s}$ when $|F_{c,s}| \ll |F_{sat,s}|$ and $F_s \approx F_{sat,s}$ when $|F_{c,s}| \gg |F_{sat,s}|$.

The electron and ion energy equations are coupled through a collisional term proportional to the Coulomb collision frequency times the difference between the temperatures of the respective species. The Coulomb collision frequency is given by

$$\nu_{ei} = \frac{16\sqrt{\pi}}{3} \frac{e^4}{m_e m_i} \left(\frac{2k_B T_e}{m_e} \right)^{-3/2} n \ln \Lambda, \quad (4.13)$$

where $\ln \Lambda \approx 20$ is the Coulomb logarithm. If the heating timescale is much greater than $1/\nu_{ei}$, the collisional timescale, then electron-ion equilibrium cannot be assumed during the heating phase. In particular, for $n \sim 10^8 \text{ cm}^{-3}$ and $T \sim 10^7 \text{ K}$, parameters typical of a nanoflare-heated coronal plasma, the collisional timescale can be estimated as $\tau_{ei,coll} \sim 1/\nu_{ei} \approx 8000 \text{ s}$. So any heating occurring on a timescale less than 8000 s will force the electron and ion populations out of equilibrium. Often when modeling

nanoflares, heating timescales of a few hundreds or even a few tens of seconds are used. Thus, treating the evolution of the electron and ions separately is particularly important when studying impulsive heating in coronal loops.

4.2 “0”-Dimensional Hydrodynamic Models

As discussed in §4.1 and §2.2.3, 1D hydrodynamic models are an invaluable tool for studying the plasma dynamics of the solar corona. However, while these models only consider evolution in the field-aligned direction, their solutions still necessitate a careful treatment of several highly-nonlinear partial differential equations. Perhaps the greatest restriction imposed on these models is the need to resolve the thermal conduction timescale, given by $\Delta t_C = 4 \times 10^{-10} n \Delta s^2 / T^{5/2}$. For a transition region plasma with an adequate grid size, this can result in a timestep on the order of several milliseconds (Bradshaw & Cargill, 2013). This makes modeling events in excess of a few hours tedious and computing thousands of field lines nearly impossible. Additionally, as 1D hydrodynamic codes become more sophisticated, incorporating features such as adaptive mesh refinement and effects due to non-equilibrium ionization, their output becomes increasingly more complicated and difficult to interpret (Cargill et al., 2012b).

Thus, there is a need for codes which a) provide an efficient way to model dynamic coronal loops and b) generate output that provides physical insight into the evolution of the plasma and the resulting physical observables. Zero-dimensional or “0D”

hydrodynamic models satisfy both of these requirements. 0D models have long been used as a tool to better understand static and dynamic coronal loop configurations. They provide a way to efficiently compute loop parameters such as T and n while incorporating the plasma processes known to be dominant in coronal loops. Most 0D loop models compute spatially-averaged time-dependent quantities and thus provide a way to perform large parameter-space surveys in reasonable amounts of time while relaxing the static equilibrium assumption.

The scaling laws of Rosner et al. (1978) are often considered some of the first 0D models as they provided simple expressions for relating the loop length, temperature, pressure, and heating rate. However, these analytic models did not provide a way to analyze loop dynamics. In the last thirty years, several 0D models have attempted to provide efficient ways to model loop dynamics. These include, but are not limited to, Fisher & Hawley (1990); Kopp & Poletto (1993); Cargill (1994); Aschwanden & Tsiklauri (2009). While many of these 0D models provided good insight into different regimes of loop evolution, Cargill et al. (2012b) show that each of these approaches has significant drawbacks when one considers the evolution of the loop throughout an entire cycle of heating and cooling. In particular, many do not treat the conductive and radiative cooling regimes correctly, do not allow for a generalized heating function, and/or do not carefully take into account the coupling between the corona and transition region.

4.2.1 The EBTEL Model

The Enthalpy-Based Thermal Evolution of Loops (EBTEL) model (Klimchuk et al., 2008; Cargill et al., 2012a) was developed initially to study nanoflare heating, but can handle a generalized heating input. EBTEL divides the loop into coronal and transition region parts, where the boundary is defined by the location at which thermal conduction switches from a source term (transition region) to a loss term (corona). The basic idea behind EBTEL, as the name implies, is to equate an enthalpy flux with any difference in magnitude between the conductive heat flux and the radiative losses from the transition region (Klimchuk et al., 2008). In this way, the processes of evaporation and condensation, the filling and draining of the coronal portion of the loop, can be accurately modeled in a 0D context.

The governing equations of the EBTEL model are derived by computing spatial averages over the coronal and transition region portions of the loop. In particular, spatial integrals of the 1D hydrostatic equations (see §2.2.3) are taken over the corona (length L) and the much thinner transition region (length $\ell \ll L$). EBTEL relies on several key assumptions: a) the flow is assumed to be subsonic, $v < C_s$, such that terms $\mathcal{O}(v^2)$ are ignored; b) the loop is shorter than a gravitational scale height such that gravitational terms are ignored; c) the ratios $c_2 = \bar{T}/T_a$ and $c_3 = T_0/T_a$, where \bar{T}, T_a, T_0 are the coronally averaged, apex, and base temperatures, respectively, are fixed such that $c_2 = 0.9$ and $c_3 = 0.6$. Additionally, as is common in loop models, only one half of the loop is computed, with symmetry about the apex assumed (Klimchuk

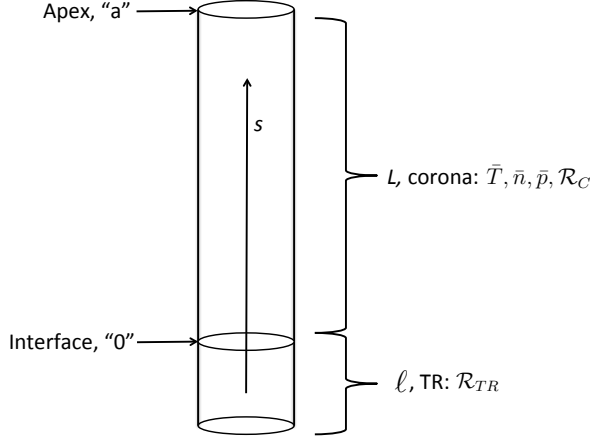


Figure 4.1 : Schematic showing how a loop half-length, with coronal portion of length L and TR length ℓ , is represented in EBTEL. Note that the loop is shown as a cylinder since (nearly) all effects due to gravitational stratification are ignored. Quantities denoted with a “0” subscript are evaluated at the corona-TR interface; quantities denoted with an “a” subscript are evaluated at the loop apex. Note that the relative size of the TR is exaggerated for the purposes of illustration and in reality $\ell \ll L$.

et al., 2008).

The 0D EBTEL equations, as given by Cargill et al. (2012a), are

$$\frac{1}{\gamma - 1} \frac{d\bar{p}}{dt} = \bar{E}_H - \frac{\mathcal{R}_C}{L}(1 + c_1), \quad (4.14)$$

$$\frac{d\bar{n}}{dt} = -\frac{c_2(\gamma - 1)}{c_3 2k_B \bar{T} L \gamma} (F_0 + c_1 \mathcal{R}_C), \quad (4.15)$$

where an overbar indicates the quantity is spatially averaged over the corona, F_0 is the heat flux at the base of the corona, $\mathcal{R}_C = \int_C ds E_R$ is the coronal spatial integral over the radiative loss term and $c_1 = \mathcal{R}_{tr}/\mathcal{R}_c$ is the ratio between the spatially integrated radiative losses over the transition region and corona, respectively. Fig.

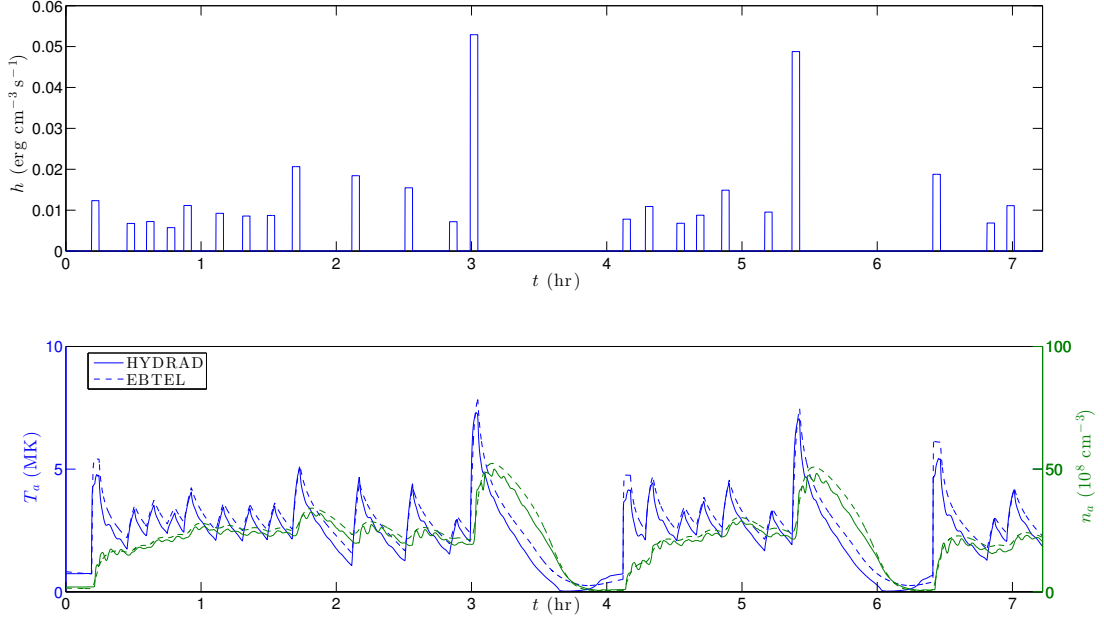


Figure 4.2 : Comparison between EBTEL (dashed) and the 1D hydrodynamic code HYDRAD (solid) for a heating function with randomly chosen start times and amplitudes chosen from a power-law distribution. The upper panel shows the heating profile, the middle panel shows the temperature profiles, and the bottom panel shows the density profiles. For both the temperature and density, the EBTEL profile follows the HYDRAD profile quite closely. For the EBTEL profiles, the apex quantities are shown here. For the HYDRAD profiles, the quantities are averaged over the upper portion of the loop.

4.1 shows the EBTEL geometry and the quantities associated with each region. The main advantage EBTEL has over other 0D codes is its treatment of the interaction between the corona and transition region. Additionally, Eqs. 4.14 and 4.15 are closed by an equation of state, $\bar{p} = 2\bar{n}k_B\bar{T}$, such that, given \bar{n} and \bar{p} , the temperature \bar{T} can be determined. It should be noted that Klimchuk et al. (2008) determined that $c_1 = 4.0$ through an empirical method based on 1D hydrodynamic simulations. Cargill et al. (2012a) later improved on this assumption by adding corrections for gravity and an improved estimate during the radiative cooling phase.

EBTEL has been carefully benchmarked with the 1D hydrodynamic code HY-

DRAD. Fig. 4.2 shows a comparison between EBTEL and HYDRAD for a series of impulsive, square heating events whose amplitudes are chosen from a power-law distribution. Cargill et al. (2012a) also provide several comparisons between EBTEL and HYDRAD for triangular, square, and gaussian heating pulses of varying duration and amplitude. Additionally, Cargill et al. (2012b) show comparisons between EBTEL, HYDRAD, and earlier 0D models in an effort to show how EBTEL improves upon previous 0D efforts by matching 1D codes in both the initial heating and subsequent cooling phases of loop evolution.

Since its initial introduction by Klimchuk et al. (2008), EBTEL has been used successfully in a large number of published studies by both modelers and observers alike. For example, Ugarte-Urra & Warren (2014) used EBTEL to forward model a series of light curves to test an event detection algorithm applied to single-pixel timeseries from active region cores. Through the use of EBTEL, they were able to determine that their algorithm could only provide an upper limit on the heating frequency as measured by transient brightenings in these light curves. Furthermore, both Qiu et al. (2012) and Liu et al. (2013) used EBTEL to analyze and constrain proposed heating functions in flaring loops. Thus, EBTEL provides an easy and powerful way to analyze coronal loops in several different regimes and produces results that are easy to compare to observations.

4.2.2 The Two-fluid EBTEL Model

While EBTEL has been an extremely useful tool for modelers and observers alike, its constituent equations (Eqs. 4.14 and 4.15) are based on the single-fluid hydrodynamic equations. As discussed in §4.1, for even mildly-impulsive heating scenarios, the electron and ion populations can be far from equilibrium during the heating phase of loop evolution, when the density is low and the temperature is high. Thus if EBTEL is going to be used to study impulsive heating in coronal loops, it should take into account these two-fluid effects.

The bulk of the work behind this thesis has been devoted to deriving and numerically implementing a set of two-fluid EBTEL equations, EBTEL-2fl hereafter. These equations are derived by applying the “EBTEL treatment,” as outlined in Klimchuk et al. (2008) and discussed in §4.2.1, to the two-fluid hydrodynamic equations (see §4.1). First, Eqs. 4.5 and 4.6 are plugged into Eqs. 4.3 and 4.4 such that

$$\frac{1}{\gamma - 1} \frac{\partial p_e}{\partial t} = -\frac{\gamma}{\gamma - 1} \frac{\partial}{\partial s}(p_e v) + v \frac{\partial p_e}{\partial s} - \frac{\partial F_e}{\partial s} + \frac{1}{\gamma - 1} k_B n \nu_{ei} (T_i - T_e) - E_R + E_{H,e}, \quad (4.16)$$

$$\frac{1}{\gamma - 1} \frac{\partial p_i}{\partial t} = -\frac{\gamma}{\gamma - 1} \frac{\partial}{\partial s}(p_i v) - v \frac{\partial p_i}{\partial s} - \frac{\partial F_i}{\partial s} + \frac{1}{\gamma - 1} k_B n \nu_{ei} (T_e - T_i) + E_{H,i}. \quad (4.17)$$

Note that in keeping with the assumptions of the original EBTEL model, the $\mathcal{O}(v^2)$ terms in Eq. 4.6 have been dropped. Next, Eq. 4.16 is integrated over the coronal

portion of the loop (i.e. from the base to the apex),

$$\int_C ds \left[\frac{1}{\gamma - 1} \frac{\partial p_e}{\partial t} = -\frac{\gamma}{\gamma - 1} \frac{\partial}{\partial s} (p_e v) + v \frac{\partial p_e}{\partial s} - \frac{\partial F_e}{\partial s} + \frac{1}{\gamma - 1} k_B n \nu_{ei} (T_i - T_e) - E_R + E_{H,e} \right]. \quad (4.18)$$

Both the heat flux and the velocity at the loop apex are neglected such that $\int_C ds \partial(p_e v)/\partial s \approx (p_e v)_0$ and $\int_C ds \partial F_e/\partial s \approx -F_{e,0}$. Plugging these expressions into Eq. 4.18 yields

$$\frac{L}{\gamma - 1} \frac{d\bar{p}_e}{dt} = \frac{\gamma}{\gamma - 1} (p_e v)_0 + F_{e,0} + \psi_C + \frac{Lk_B}{\gamma - 1} \bar{n} \bar{\nu}_{ei} (\bar{T}_i - \bar{T}_e) - \mathcal{R}_C + L \bar{E}_{H,e}, \quad (4.19)$$

where $\psi_C = \int_C ds v \partial p_e / \partial s$ and $\bar{\nu}_{ei}$ is evaluated at \bar{n} and \bar{T}_e . The case of the ion energy is exactly analogous such that Eq. 4.17, when averaged over the corona, becomes

$$\frac{L}{\gamma - 1} \frac{d\bar{p}_i}{dt} = \frac{\gamma}{\gamma - 1} (p_i v)_0 + F_{0,i} - \psi_C + \frac{Lk_B}{\gamma - 1} \bar{n} \bar{\nu}_{ei} (\bar{T}_e - \bar{T}_i) + L \bar{E}_{H,i}. \quad (4.20)$$

In order to be able to solve Eqs. 4.19 and 4.20, the enthalpy flux at the base of the corona for both the electrons and ions, $(p_e v)_0$ and $(p_i v)_0$, must be determined. Instead of integrating over the coronal, Eq. 4.16 is instead integrated over the transition region

such that

$$\int_{TR} ds \left[\frac{1}{\gamma-1} \frac{\partial p_e}{\partial t} = -\frac{\gamma}{\gamma-1} \frac{\partial}{\partial s} (p_e v) + v \frac{\partial p_e}{\partial s} - \frac{\partial F_{c,e}}{\partial s} + \frac{1}{\gamma-1} k_B n \nu_{ei} (T_i - T_e) - E_R + E_{H,e} \right], \quad (4.21)$$

$$\frac{\ell}{\gamma-1} \frac{d \bar{p}_e}{dt} = -\frac{\gamma}{\gamma-1} (p_e v)_0 - F_{0,e} + \psi_{TR} + \frac{\ell k_B}{\gamma-1} \bar{n} \bar{\nu}_{ei} (\bar{T}_i - \bar{T}_e) - \mathcal{R}_{TR} + \ell \bar{E}_{H,e}, \quad (4.22)$$

where $\psi_{TR} = \int_{TR} ds v \partial p_e / \partial s$ and an overbar indicates an average over the transition region. However, since $\ell \ll L$, all terms $\mathcal{O}(\ell)$ are neglected such that the expression for the electron enthalpy flux becomes,

$$\frac{\gamma}{\gamma-1} (p_e v)_0 = -F_{e,0} + \psi_{TR} - \mathcal{R}_{TR}. \quad (4.23)$$

Again, the ion case is exactly analogous such that the ion enthalpy flux can be written,

$$\frac{\gamma}{\gamma-1} (p_i v)_0 = -F_{0,i} - \psi_{TR}. \quad (4.24)$$

Plugging Eqs. 4.23 and 4.24 into Eqs. yields the electron and ion EBTEL-2fl pressure equations,

$$\frac{d}{dt} \bar{p}_e = \frac{\gamma-1}{L} [\psi_{TR} + \psi_C - (\mathcal{R}_{TR} + \mathcal{R}_C)] + k_B \bar{n} \nu_{ei} (\bar{T}_i - \bar{T}_e) + (\gamma-1) \bar{E}_{H,e}, \quad (4.25)$$

$$\frac{d}{dt} \bar{p}_i = -\frac{\gamma-1}{L} (\psi_{TR} + \psi_C) + k_B \bar{n} \nu_{ei} (\bar{T}_e - \bar{T}_i) + (\gamma-1) \bar{E}_{H,i}. \quad (4.26)$$

Note that Eq. 4.25 + Eq. 4.26 = Eq. 4.14. Thus, the original single-fluid EBTEL pressure equation can be recovered from the electron and ion EBTEL-2fl pressure equations.

Now, to derive the EBTEL-2fl density equation, Eq. 4.1, using $\rho \approx m_i n$, is integrated over the coronal portion of the loop,

$$\int_C ds \left[\frac{\partial n}{\partial t} + \frac{\partial(nv)}{\partial s} = 0 \right], \quad (4.27)$$

$$L \frac{d\bar{n}}{dt} = - \int_C ds \frac{\partial(nv)}{\partial s} = (nv)_0, \quad (4.28)$$

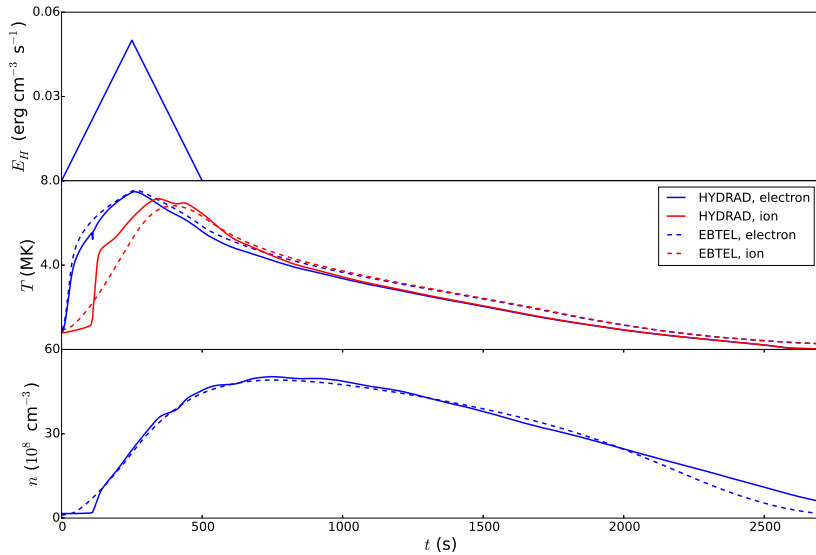
where again it is assumed that the velocity vanishes at the apex of the loop. Additionally, the right-hand side can be approximated $(nv)_0 \approx n_0 v_0$ and using Eq. 4.7,

$$L \frac{d\bar{n}}{dt} = \frac{p_{e,0} v_0}{k_B T_{e,0}}. \quad (4.29)$$

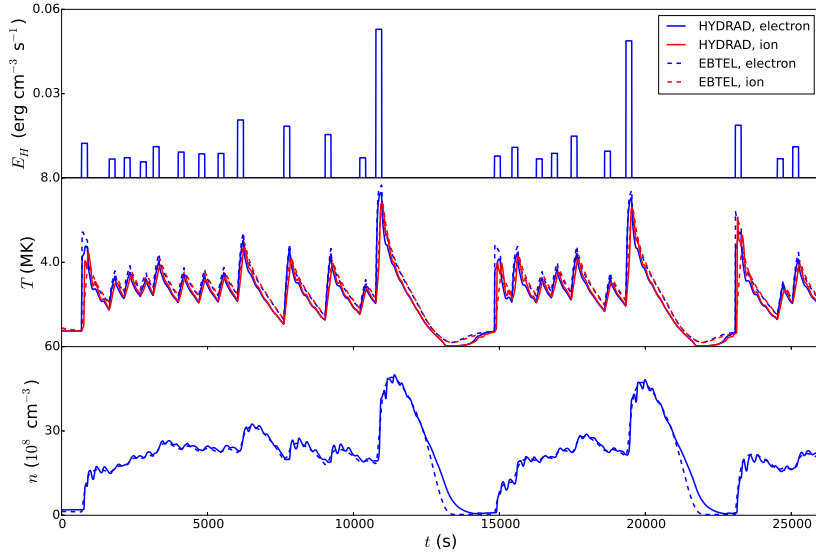
Finally, approximating $p_{e,0} v_0 \approx (p_e v)_0$ and using Eq. 4.23, the EBTEL-2fl density equation can be expressed as,

$$\frac{d\bar{n}}{dt} = \frac{c_2(\gamma - 1)}{c_3 \gamma L k_B \bar{T}_e} (\psi_{TR} - F_{e,0} - \mathcal{R}_{TR}), \quad (4.30)$$

where the substitution $T_{e,0} = c_3 \bar{T}/c_2$ has been used. Thus, Eqs. 4.25, 4.26, and 4.30 are the EBTEL-2fl equations for pressure and density evolution and are closed by the equations of state, Eqs. 4.7 and 4.8.



(a)



(b)

Figure 4.3 : Comparisons between the EBTEL-2fl model (dashed) and HYDRAD (solid) for (a) a single triangular pulse lasting 500 s and (b) the same heating profile as in Fig. 4.2. The upper panels show the heating profiles, the middle panels show the electron (blue) and ion (red) temperature profiles, and the bottom panels show the density profiles.

Looking back to Eqs. 4.25, 4.26, and 4.30, one may notice that there are still two missing pieces: ψ_C and ψ_{TR} . These terms arise from the spatial integrals over the electron pressure gradients that represent the work done by the electric field on the species (the mobile electrons in this case) to maintain quasi-neutrality. To derive ψ_{TR} , first consider the quantity $\xi \equiv T_{e,0}/T_{i,0}$. Then, using Eq. 4.7, multiplying by $1 = v_0/v_0$, and again the approximation $p_{e,0}v_0 \approx (p_e v)_0$,

$$\xi \equiv \frac{T_{e,0}}{T_{i,0}} = \frac{(p_e v)_0}{(p_i v)_0}. \quad (4.31)$$

Plugging in Eqs. 4.23 and 4.24 and using a bit of algebra, an expression for ψ_{TR} can be derived,

$$\psi_{TR} = \frac{1}{1 + \xi} (F_{0,e} + \mathcal{R}_{TR} - \xi F_{0,i}). \quad (4.32)$$

Additionally, ψ_C is approximated as,

$$\psi_C = \int_C ds v \frac{\partial p_e}{\partial s} \approx \bar{v} p_e^{(a)} - (p_e v)_0. \quad (4.33)$$

Thus, Eqs. 4.32 and 4.33 provide the final pieces for the set of EBTEL-2fl equations. Additionally, note that, using Eq. 4.32, $\psi_{TR} - F_{e,0} - \mathcal{R}_{TR} = -\xi(F_{i,0} + F_{e,0} + \mathcal{R}_{TR})/(1 + \xi)$. In the single-fluid limit, $\bar{T}_e = \bar{T}_i = \bar{T}$ or $\xi = 1$, noting that $F_0 = F_e + F_i$, it can be seen that $\psi_{TR} - F_{e,0} - \mathcal{R}_{TR} = -(F_0 + \mathcal{R}_{TR})/2$ such that the original EBTEL equation, Eq. 4.15, is recovered from Eq. 4.30. Thus, all three of the EBTEL-2fl equations reduce to the original single-fluid EBTEL equations in the limit of electron-

ion equilibrium.

As with the original EBTEL model, EBTEL-2fl has been carefully benchmarked against the HYDRAD hydrodynamic code. Fig. 4.3 shows a comparison between EBTEL-2fl and HYDRAD for two different heating functions. Fig. 4.3(a) shows the responses of EBTEL-2fl and HYDRAD to a single triangular pulse with a duration of 500 s. Note that the density evolution matches quite well during both the heating phase and cooling phase. A noticeable discrepancy occurs between the two ion temperatures at the start of the heating phase. The EBTEL-2fl ion temperature tends to rise more quickly because the density increases more quickly, initially in the EBTEL model. Since the electron-ion coupling term $\propto n^2$, the ions couple more quickly to the heated electrons. This artificial density increase is a consequence of the 0D nature of the model: in a loop with spatial extent, there is an additional lag in the density increase due to the inertia of the plasma. However, in EBTEL-2fl, the “loop” has no spatial extent and so the plasma essentially begins moving up the loop in zero time. Additionally, 4.3(b) shows the EBTEL-2fl response in density and temperature for a series of 200 s heating events. The \bar{n} , \bar{T}_e , \bar{T}_i profiles all track quite well relative to the HYDRAD profiles.

4.3 Numerical Implementation

While the original EBTEL model of Klimchuk et al. (2008); Cargill et al. (2012a) was coded in the Interactive Data Language (IDL), a popular software package in

solar physics, EBTEL-2fl has been implemented in the C programming language. The reason for this is twofold: 1) C offers a significant speedup over IDL, allowing for much more efficient parameter space explorations. For example, a 10,000 second run of the original EBTEL model can take up to 7 seconds, while an equivalent case in EBTEL-2fl takes only a fraction of a second. 2) C is freely available on all computing platforms while a department-wide IDL license could cost upwards of several hundred dollars. Since this code will eventually be distributed to the solar physics community, all researchers will be able to use the code regardless of the financial situation of their department or university. Additionally, C is in general more portable than proprietary languages like IDL, meaning that EBTEL-2fl can easily be run on large computing clusters, making parameter space investigations even more efficient.

Though the original EBTEL code used only a simple Euler solver, with a static timestep, the EBTEL-2fl model includes a slightly more sophisticated solver with an optional adaptive timestepping routine. The code also includes an option to use a simple Euler. Below, both the Euler and fourth-order Runge-Kutta solvers will be briefly described. Additionally, details of the adaptive timestep routine will also be discussed.

4.3.1 Euler Method

Perhaps the first step in any numerical ordinary differential equation (ODE) solution is the explicit Euler method. For an ODE of the form,

$$\frac{dy_i}{dt} = f(y_1(t), \dots, y_i(t), \dots, y_N(t); t), \quad y_i(t=0) = y_{i,0} \quad \text{for } i = 1, \dots, N, \quad (4.34)$$

a first-order Euler solver for y_i can be written as

$$y_{i,j+1} = y_{i,j} + \tau f(y_{1,j}, \dots, y_{i,j}, \dots, y_{N,j}; t_j), \quad (4.35)$$

where $\tau = t_{j+1} - t_j$ and j is the index representing the current timestep. The index i represents the number of quantities to be solved such that the right-hand side of Eq. 4.34 can depend on all or none of the other quantities. In the case of the EBTEL-2f model, $N = 3$ and $y_1, y_2, y_3 = p_e, p_i, n$. Note also that the EBTEL-2f equations, Eqs. 4.25, 4.26, and 4.30 all have the format of Eq. 4.34 with the values at $t = 0$ being determined by static equilibrium conditions.

4.3.2 Fourth-order Runge-Kutta Method

While Euler solvers are easy to implement (see §4.3.1) they often suffer from a lack of accuracy and stability (Press, 1992). Recall that for a first-order Euler scheme, the global truncation error will be $\mathcal{O}(\tau)$. Thus, sufficiently small timesteps are needed to ensure an accurate solution. However, the smaller the timestep, the longer the

compute time. The widely-used fourth-order Runge-Kutta method, RK4 hereafter, improves accuracy and stability by calculating the right-hand side of Eq. 4.34 at intermediate points between t and $t + \tau$. In particular, RK4 uses an Euler method to calculate the f at $t + \tau/2$. The value of y_i is then estimated at $t + \tau/2$ using this Euler method value of f at $t + \tau/2$ and this new value of y_i is used to estimate f at $t + \tau$. The RK4 method for equations of the form of Eq. 4.34 is given by,

$$y_{i,j+1} = y_{i,j} + \frac{1}{6}(k_1 + 2k_2 + 2k_3 + k_4) + \mathcal{O}(\tau^5), \quad (4.36)$$

where

$$k_1 = \tau f(y_1(t_j), \dots, y_N(t_j); t_j), \quad (4.37)$$

$$k_2 = \tau f(y_1(t_j) + k_1/2, \dots, y_N(t_j) + k_1/2; t_j + \tau/2), \quad (4.38)$$

$$k_3 = \tau f(y_1(t_j) + k_2/2, \dots, y_N(t_j) + k_2/2; t_j + \tau/2), \quad (4.39)$$

$$k_4 = \tau f(y_1(t_j) + k_3, \dots, y_N(t_j) + k_3; t_j + \tau), \quad (4.40)$$

(Press, 1992). For a static timestep, where the total number of steps is (total time)/ τ , the global truncation error will be $\mathcal{O}(h^4)$. Thus, Eqs. 4.25, 4.26, and 4.30 can be solved using Eq. 4.36 with greater accuracy than with Eq. 4.35.

4.3.3 Adaptive Timestep Routine

During the heating phase of a loop evolution cycle, particularly in an impulsive heating scenario, the temperature gradient in time can become very steep, especially if the density at the onset of heating is low (e.g. when the time between heating events is longer than the radiative cooling/draining timescale). Alternatively, during the radiative cooling phase, these temperature gradients are relatively shallow. Thus, very short timesteps will ensure adequate resolution of the behavior during the heating phase, but will lead to unnecessarily long compute times during the radiative cooling phase. On the other hand, using a long timestep will ensure small compute times, but could, at best, lead to an incorrect treatment of the fast-acting thermal conduction during the heating phase, and, at worst, cause serious stability issues in the solution during this period.

Thus, Eqs. 4.25 and 4.26 lend themselves to an adaptive timestepping approach, where the timestep, τ , is adjusted based on how the solution is changing at time t_j . There are many different timestepping control techniques; EBTEL-2fl uses the approach as outlined in Garcia (2000). Consider two cases of advancing the solution $y_{i,j}$ to $y_{i,j+1}$: 1) take one big timestep τ such that the final value is $y_{i,j+1}^{(b)}$; 2) take two small timesteps $\tau/2$ such that $y_i(t_j + \tau/2)$ is used to determine $y_i(t_j + \tau) = y_{i,j+1}^{(s)}$. To determine whether this error is acceptable, define $\Delta_c \equiv |y_{i,j+1}^{(b)} - y_{i,j+1}^{(s)}|$. Then,

given some acceptable, user-specified error Δ_i , the error ratio can be defined

$$\epsilon = \frac{\Delta_c}{\Delta_i}. \quad (4.41)$$

Recalling that the local truncation error for the RK4 method is $\Delta \propto \tau^5$, the new timestep can be defined as

$$\tau_{new} = \tau \epsilon^{-1/5}, \quad (4.42)$$

where τ is the original timestep. If $\epsilon < 1$, this new timestep is accepted. If $\epsilon > 1$, the whole process is repeated with $\tau = \tau_{new}$. If the $\epsilon < 1$ criteria is not met in some finite number of iterations, the routine fails.

Chapter 5

Results

This chapter will include the results of our numerical study. Here we will also describe how the study was performed and what tools were used to perform the study. It is best not to introduce any new tools here; just pool from those that have already been discussed and show how they were applied. Show lots of plots and tables.

As discussed in §2.2 and §3.3, hydrodynamic loop models are an invaluable tool for constraining heating properties in the solar corona. In particular, this thesis has focused on developing an efficient two-fluid hydrodynamic model, EBTEL-2fl (see §4.2.2), to study the effect of various heating parameters on the emission measure in active region cores. The 0D nature and consequentially short run times of the EBTEL-2fl code allow for the exploration of a large parameter space. This thesis has used the newly-developed EBTEL-2fl code to examine the effects of varying heating frequency, loop length, heating amplitude power-law distribution index, and preferentially heated species on the emission measure and the resulting hotward and coolward emission measure slopes (see §3.2.2). Altogether, this amounts to a $20 \times 3 \times 3 \times 3$ parameter space for electron and ion heating as well as the single-fluid case.

Each EBTEL-2fl run has a simulation time of 80,000 s, with initial conditions determined via static loop solutions (see 2.2.1). Flux-limiting (see Eqs. 4.11 and

4.12) is used so as to more accurately model cooling by thermal conduction in the early heating phase. The Raymond-Klimchuk power-law loss function (see Eq. RAD LOSS EQ HERE) is used to model the volumetric radiative losses. In §5.1, the various heating functions used in the EBTEL-2fl runs are discussed. Next, in §5.2 and §5.3, the resulting emission measure curves for the electron- and ion-heating cases are shown. Finally, in §5.4, equivalent results for the original single-fluid EBTEL model are shown so as to better elucidate the effects of two-fluid models on forward-modeled emission.

5.1 Heating Functions

As seen in Fig. 4.3, heating functions in EBTEL-2fl are defined in terms of discrete heating events in units of ergs $\text{cm}^{-3} \text{ s}^{-1}$, a volumetric heating rate. Additionally, a static background heating rate of $H_b = 3.4 \times 10^{-6}$ is applied to ensure that the loop does not drop to unphysically low temperatures and densities between heating events. All of the heating functions presented here are composed of triangular pulses with a fixed duration of $\tau_H = 100$ s, a relatively impulsive event. Thus, for loop length L and cross-sectional area A , the total energy per event is $Q_i = LAH_i\tau_H/2$, where H_i is the heating rate amplitude for the i th event. Thus, each run will consist of N heating events, each of peak amplitude H_i with a steady background value of H_b .

Observations have suggested that EM distributions in active region cores are peaked near 4 MK (Warren et al., 2011, 2012). This means that the loops in these

active region cores are maintained at an equilibrium temperature of $T_{peak} \approx 4$ MK.

The corresponding heating rate can be estimated using the hydrostatic equations.

Using Eq. HYDROSTATIC EQ REF HERE, neglecting the radiative loss term and letting $dF_C/ds \approx \kappa_0 T_{peak}^{7/2}/L^2$, $E_{H,eq}$ can be estimated as

$$E_{H,eq} = \frac{\kappa_0 T_{peak}^{7/2}}{L^2}. \quad (5.1)$$

In the context of loop dynamics, $E_{H,eq}$ can be interpreted as a time-averaged volumetric heating rate. Thus, to maintain an emission measure peaked about T_{peak} , the individual heating rates are constrained by

$$E_{H,eq} = \frac{\tau_H}{2T} \sum_{i=1}^N H_i. \quad (5.2)$$

Note that if $H_i = H_0$ for all i , the uniform heating amplitude H_0 is just $H_0 = 2TE_{H,eq}/N\tau_H$. Thus, for $L = 40$ Mm, $A = 10^{14}$ cm 2 , the total amount of energy injected into the loop by one heating event for a loop heated by $N = 20$ nanoflares in $T = 80000$ s is $Q = LATE_{H,eq}/N \approx 1.3 \times 10^{25}$, consistent with the energy budget of the Parker nanoflare model discussed in §1.3.2 (Cargill, 2014).

As discussed in 2.1, determining the heating frequency in active region cores will help to place constraints on the source(s) of heat in the corona. Here, the heating frequency is defined in terms of the waiting time, T_N , between successive heating events. Following Cargill (2014), the range of waiting times is $250 \leq T_N \leq 5000$ s

in increments of 250 s, for a total of 20 different possible heating frequencies. Additionally, T_N can be written as $T_N = (T - N\tau_H)/N$, where $T = 80000$ s is the total simulation time. Note that because T and τ_H are fixed, as T_N increases, N decreases. Correspondingly, Q_i , the energy injected per event, increases according to Eq. 5.2 such that the total energy injected per run is constant, regardless of T_N .

Regarding the peak heating rate per event, two different possibilities are explored: 1) uniform heating rate such that $H_i = H_0$ for all i and 2) H_i chosen from a power-law distribution with index α where $\alpha = -1.5, -2.0, -2.5$. For the second case, it should be noted that, when T_N is large, $N \sim 20$ events, meaning a single run does not accurately represent the distribution of index α . Thus, a sufficiently large number of runs, N_{MC} , are computed for each T_N to ensure that the total number of events is $N_{tot} = N \times N_{MC} \sim 10^4$ such that the distribution is well-represented. Fig. 5.1 shows the resulting distribution for $T_N = 5000$ s with a specified index of $\alpha = -1.5$.

Thus far, T_N and H_i have been treated independently. However, as discussed in 1.3.2, the twisted and stressed coronal field is thought to contribute to the supposed bursty heating of the corona. Following Cargill (2014), a model in which $Q_i \propto T_{N,i}^b$ is considered, where $Q_i, T_{N,i}$ are the total energy and waiting time following the i th event and $b = 1, 2$. The reasoning for such an expression is as follows. Bursty, nanoflare heating is thought to arise from the stressing and subsequent relaxation of the field. If a sufficient amount of time has elapsed since the last energy release event, the field will have had enough time to “wind up” such that the subsequent energy release is

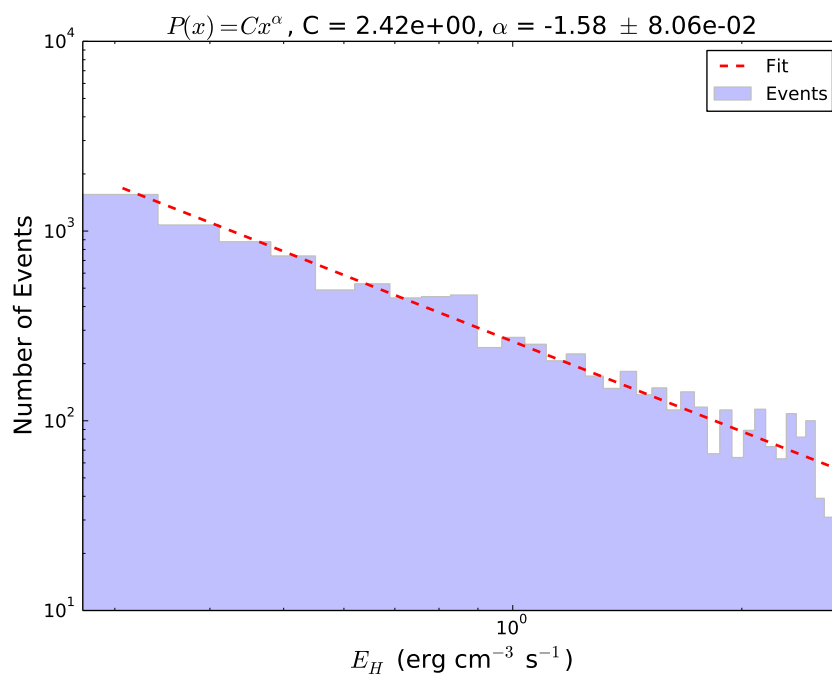


Figure 5.1 : Distribution of event energies for $L = 40$ Mm, $\alpha = -1.5$, $T_N = 5000$ s. While each run only includes ~ 16 events, 625 runs are computed such that $N_{tot} \sim 10^4$. The dashed red line shows the power-law fit to the resulting event distribution. The resulting α value from the fit is in good agreement with the specified value.

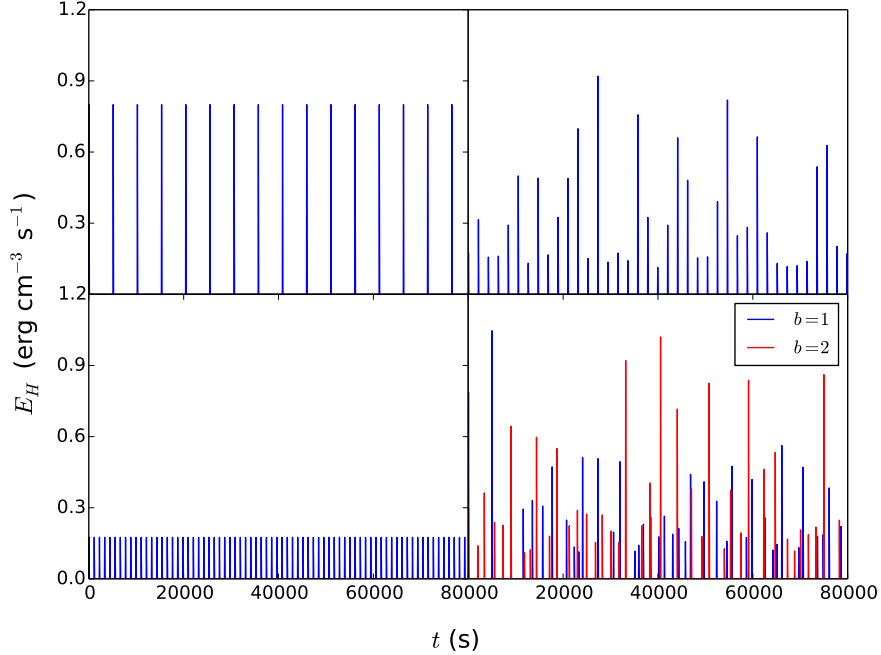


Figure 5.2 : All heating functions are for $L = 40$ Mm. Starting counter-clockwise from the bottom left: uniform heating amplitudes for $T_N = 1000$ s; uniform heating amplitudes for $T_N = 5000$ s; power-law distributed heating amplitudes for $\alpha = -1.5$, $T_N = 2000$ s; power-law distributed amplitudes for $\alpha = -1.5$ where the wait times depend on the event energies and the mean wait time for both b values is $\langle T_N \rangle = 2000$ s.

large. Conversely, if only a small amount of time has elapsed since the last event, the field will have not had time to become as stressed, resulting in a lower energy event. Thus, this scaling provides a way to incorporate a more realistic heating function into a hydrodynamic model which cannot self-consistently determine the heat input based on the evolving magnetic field. Fig. 5.2 shows the various heating functions used for a variety of T_N values.

5.2 Electron Heating

For each section, show L=40, all alpha, b=1,2

5.3 Ion Heating

5.4 Single-fluid Comparisons

Chapter 6

Conclusions

This chapter will discuss the conclusions that we can draw based on the results in the results section. What do these results mean? What are the implications in the context of loops in active region cores? May include some topics for future work in this section as well or just wait and put it in a different chapter

Appendix A

Coronal and Transition Region Pressure Gradient Integrals

An appendix will go here.

Appendix B

Additional Plots

More plots will go here

Bibliography

Alfvén, H. 1941, Arkiv foor Matematik, Astronomi och Fysik, 27A

Aschwanden, M. J. 2006, Physics of the Solar Corona: An Introduction with Problems and Solutions, 2nd edn., Springer-Praxis Books in Geophysical Sciences (Berlin ; New York: Springer)

Aschwanden, M. J., & Tsiklauri, D. 2009, The Astrophysical Journal Supplement Series, 185, 171

Bradshaw, S. J., & Cargill, P. J. 2006, Astronomy and Astrophysics, 458, 987

—. 2013, The Astrophysical Journal, 770, 12

Bradshaw, S. J., & Klimchuk, J. A. 2011, The Astrophysical Journal Supplement Series, 194, 26

Bradshaw, S. J., Klimchuk, J. A., & Reep, J. W. 2012, The Astrophysical Journal, 758, 53

Bradshaw, S. J., & Raymond, J. 2013, Space Science Reviews, 178, 271

Brosius, J. W., Daw, A. N., & Rabin, D. M. 2014, The Astrophysical Journal, 790, 112

- Cargill, P. J. 1994, *The Astrophysical Journal*, 422, 381
- . 2014, *The Astrophysical Journal*, 784, 49
- Cargill, P. J., Bradshaw, S. J., & Klimchuk, J. A. 2012a, *The Astrophysical Journal*, 752, 161
- . 2012b, *The Astrophysical Journal*, 758, 5
- Cargill, P. J., & Klimchuk, J. A. 2004, *The Astrophysical Journal*, 605, 911
- Carroll, B. W., & Ostlie, D. A. 2007, *An Introduction to Modern Astrophysics*, 2nd edn. (San Francisco: Pearson)
- Cheung, M. C. M., & Isobe, H. 2014, *Living Reviews in Solar Physics*, 11, 3
- Cirtain, J. W., Golub, L., Winebarger, A. R., et al. 2013, *Nature*, 493, 501
- De Moortel, I., Hood, A. W., Ireland, J., & Walsh, R. W. 2002a, *Solar Physics*, 209, 89
- De Moortel, I., Ireland, J., Walsh, R. W., & Hood, A. W. 2002b, *Solar Physics*, 209, 61
- De Pontieu, B., McIntosh, S. W., Carlsson, M., et al. 2011, *Science*, 331, 55
- Dere, K. P., Landi, E., Mason, H. E., Fossi, B. C. M., & Young, P. R. 1997, *Astronomy and Astrophysics Supplement Series*, 125, 25
- Drake, J. F., & Swisdak, M. 2014, *Physics of Plasmas (1994-present)*, 21, 072903

- Edlén, B. 1943, Zeitschrift für Astrophysik, 22, 30
- Fisher, G. H., & Hawley, S. L. 1990, The Astrophysical Journal, 357, 243
- Garcia, A. L. 2000, Numerical Methods for Physics, 2nd edn. (New Jersey: Prentice Hall), bibliography note: Includes bibliographical references (pages 399-406) and index Held by: FONDREN
- Gary, G. A. 2001, Solar Physics, 203, 71
- Gary, G. A., West, E. A., Rees, D., et al. 2007, Astronomy and Astrophysics, 461, 707
- Gold, T. 1964, NASA Special Publication, 50, 389
- Golub, L., & Pasachoff, J. M. 2010, The Solar Corona (Cambridge, UK ; New York : Cambridge University Press, 2010.)
- Grotian, W. 1939, Naturwissenschaften, 27
- Jordan, C. 1980, Astronomy and Astrophysics, 86, 355
- Karpen, J. T., & DeVore, C. R. 1987, The Astrophysical Journal, 320, 904
- Kashyap, V., & Drake, J. J. 1998, The Astrophysical Journal, 503, 450
- Klimchuk, J. A. 2006, Solar Physics, 234, 41
- Klimchuk, J. A., Patsourakos, S., & Cargill, P. J. 2008, The Astrophysical Journal, 682, 1351

- Kobayashi, K., Cirtain, J., Golub, L., et al. 2011, in Society of Photo-Optical Instrumentation Engineers (SPIE) Conference Series, Vol. 8147, 81471M
- Kopp, R. A., & Poletto, G. 1993, *The Astrophysical Journal*, 418, 496
- Krieger, A., Paolini, F., Vaiana, G. S., & Webb, D. 1972, *Solar Physics*, 22, 150
- Landi, E., Feldman, U., & Dere, K. P. 2002, *The Astrophysical Journal Supplement Series*, 139, 281
- Landi, E., & Klimchuk, J. A. 2010, *The Astrophysical Journal*, 723, 320
- Landi, E., Reale, F., & Testa, P. 2012, *Astronomy and Astrophysics*, 538, A111
- Landi, E., Young, P. R., Dere, K. P., Del Zanna, G., & Mason, H. E. 2013, *The Astrophysical Journal*, 763, 86
- Liu, W.-J., Qiu, J., Longcope, D. W., & Caspi, A. 2013, *The Astrophysical Journal*, 770, 111, arXiv:1304.4521 [astro-ph]
- Luciani, J. F., Mora, P., & Virmont, J. 1983, *Physical Review Letters*, 51, 1664
- Markovskii, S. A., & Hollweg, J. V. 2004, *The Astrophysical Journal*, 609, 1112
- Mason, H. E., & Fossi, B. C. M. 1994, *Astronomy and Astrophysics Review*, 6, 123
- Metropolis, N., Rosenbluth, A. W., Rosenbluth, M. N., Teller, A. H., & Teller, E. 1953, *The Journal of Chemical Physics*, 21, 1087

- Mulu-Moore, F. M., Winebarger, A. R., & Warren, H. P. 2011, *The Astrophysical Journal Letters*, 742, L6
- Olson, R. J. M., & Pasachoff, J. M. 2007, *Religion & the Arts*, 11, 299
- Ono, Y., Yamada, M., Akao, T., Tajima, T., & Matsumoto, R. 1996, *Physical Review Letters*, 76, 3328
- Parker, E. N. 1955, *The Astrophysical Journal*, 121, 491
- . 1957, *Journal of Geophysical Research*, 62, 509
- . 1963, *The Astrophysical Journal Supplement Series*, 8, 177
- . 1983a, *The Astrophysical Journal*, 264, 642
- . 1983b, *The Astrophysical Journal*, 264, 635
- . 1988, *The Astrophysical Journal*, 330, 474
- Peter, H., & Dwivedi, B. N. 2014, *Stellar and Solar Physics*, 1, 2
- Petschek, H. E. 1964, *NASA Special Publication*, 50, 425
- Press, W. H. 1992, *Numerical Recipes in C: the Art of Scientific Computing*, 2nd edn. (Cambridge, UK ; New York: Cambridge University Press)
- Priest, E. R., & Forbes, T. 2000, *Magnetic Reconnection: MHD Theory and Applications* (Cambridge, UK; New York: Cambridge University Press)

- Qiu, J., Liu, W.-J., & Longcope, D. W. 2012, *The Astrophysical Journal*, 752, 124
- Reale, F. 2010, *Living Reviews in Solar Physics*, 7, 5
- Reale, F., & Orlando, S. 2008, *The Astrophysical Journal*, 684, 715
- Reale, F., Testa, P., Klimchuk, J. A., & Parenti, S. 2009, *The Astrophysical Journal*, 698, 756
- Reep, J. W., Bradshaw, S. J., & Klimchuk, J. A. 2013, *The Astrophysical Journal*, 764, 193
- Rosner, R., Tucker, W. H., & Vaiana, G. S. 1978, *The Astrophysical Journal*, 220, 643
- Schmelz, J. T., & Pathak, S. 2012, *The Astrophysical Journal*, 756, 126
- Schmelz, J. T., Saar, S. H., DeLuca, E. E., et al. 2009, *The Astrophysical Journal Letters*, 693, L131
- Spitzer, L., & Härm, R. 1953, *Physical Review*, 89, 977
- Sweet, P. A. 1958, in *Electromagnetic Phenomena in Cosmical Physics*, Vol. 6 (Cambridge University Press), 123
- Testa, P., De Pontieu, B., Martínez-Sykora, J., et al. 2013, *The Astrophysical Journal Letters*, 770, L1
- Testa, P., De Pontieu, B., Allred, J., et al. 2014, *Science*, 346, 1255724

- Tripathi, D., Klimchuk, J. A., & Mason, H. E. 2011, *The Astrophysical Journal*, 740, 111
- Ugarte-Urra, I., & Warren, H. P. 2014, *The Astrophysical Journal*, 783, 12
- Vaiana, G. S., Krieger, A. S., & Timothy, A. F. 1973, *Solar Physics*, 32, 81
- Vaiana, G. S., Reidy, W. P., Zehnpfennig, T., van Speybroeck, L., & Giacconi, R. 1968, *Science*, 161, 564
- Warren, H. P., Brooks, D. H., & Winebarger, A. R. 2011, *The Astrophysical Journal*, 734, 90
- Warren, H. P., Winebarger, A. R., & Brooks, D. H. 2012, *The Astrophysical Journal*, 759, 141
- Winebarger, A. R. 2014, *AGU Fall Meeting Abstracts*, 52, 03
- Winebarger, A. R., Schmelz, J. T., Warren, H. P., Saar, S. H., & Kashyap, V. L. 2011, *The Astrophysical Journal*, 740, 2
- Winebarger, A. R., Warren, H. P., Schmelz, J. T., et al. 2012, *The Astrophysical Journal Letters*, 746, L17
- Withbroe, G. L., & Noyes, R. W. 1977, *Annual Review of Astronomy and Astrophysics*, 15, 363
- Yoo, J., Yamada, M., Ji, H., Jara-Almonte, J., & Myers, C. E. 2014, *Physics of Plasmas (1994-present)*, 21, 055706